Scale Interactions between the MJO and the Western Maritime Continent

C. E. BIRCH,*,+ S. WEBSTER,# S. C. PEATMAN,@ D. J. PARKER,+ A. J. MATTHEWS,& Y. LI,** M. E. E. HASSIM++

* *Met Office@Leeds, University of Leeds, Leeds, United Kingdom*
+ *School of Earth and Environment, University of Leeds, Leeds, United Kingdom*
# *Met Office, Exeter, United Kingdom*
@ *University of Reading, Reading, United Kingdom*
& *Centre for Ocean and Atmospheric Sciences, School of Environmental Sciences, and School of Mathematics, University of East Anglia, Norwich, United Kingdom*
** *ARC Centre of Excellence for Climate System Science, and Climate Change Research Centre, University of New South Wales, Sydney, New South Wales, Australia*
++ *Centre for Climate Research Singapore, Meteorological Service Singapore, Singapore*

(Manuscript received 3 August 2015, in final form 20 November 2015)

ABSTRACT

State-of-the-art regional climate model simulations that are able to resolve key mesoscale circulations are used, for the first time, to understand the interaction between the large-scale convective environment of the MJO and processes governing the strong diurnal cycle over the islands of the Maritime Continent (MC). Convection is sustained in the late afternoon just inland of the coasts because of sea breeze convergence. Previous work has shown that the variability in MC rainfall associated with the MJO is manifested in changes to this diurnal cycle; land-based rainfall peaks before the active convective envelope of the MJO reaches the MC, whereas oceanic rainfall rates peak while the active envelope resides over the region. The model simulations show that the main controls on oceanic MC rainfall in the early active MJO phases are the large-scale environment and atmospheric stability, followed by high oceanic latent heat flux forced by high near-surface winds in the later active MJO phases. Over land, rainfall peaks before the main convective envelope arrives (in agreement with observations), even though the large-scale convective environment is only moderately favorable for convection. The causes of this early rainfall peak are strong convective triggers from land–sea breeze circulations that result from high surface insolation and surface heating. During the peak MJO phases cloud cover increases and surface insolation decreases, which weakens the strength of the mesoscale circulations and reduces land-based rainfall, even though the large-scale environment remains favorable for convection at this time. Hence, scale interactions are an essential part of the MJO transition across the MC.

1. Introduction

The Maritime Continent (MC) is located in the tropical warm pool and consists of many hundreds of islands with complex coastlines and topography, shallow seas, and high sea surface temperatures (SSTs). It is one of the wettest places on Earth, and the high latent heat release from organized convective activity in the region influences global circulation and climate via downstream Rossby wave responses (Jin and Hoskins 1995; Neale and Slingo 2003). On a diurnal time scale, precipitation forms over the islands in the afternoon as a result of a sea-breeze convergence mechanism and propagates offshore overnight through the reversal of the sea breeze and coupling to gravity waves (Saito et al. 2001; Mori et al. 2004; Qian 2008; Love et al. 2011; Hassim et al. 2016).

The MJO is the dominant component of intraseasonal variability in the tropics, consisting of large-scale eastward-moving convective and circulation anomalies that originate over the Indian Ocean and propagate over the MC into the western Pacific with a period of 30–90 days (Zhang 2005). Detailed understanding and accurate simulation of the complex processes within the MJO as it interacts with the MC are necessary ingredients for a successful medium-range weather forecast. However, global circulation models (GCMs) struggle to reproduce the rainfall characteristics of the MC region (Johnson

Corresponding author address: Cathryn Birch, School of Earth and Environment, University of Leeds, Woodhouse Lane, Leeds LS2 9JT, United Kingdom.
E-mail: c.e.birch@leeds.ac.uk

DOI: 10.1175/JCLI-D-15-0557.1

et al. 2016), the propagation of the MJO (Lin et al. 2006; Kim et al. 2011), and their interaction (Peatman et al. 2015). Rainfall biases develop within the first few days of a simulation (Martin et al. 2006), indicating that the key model biases relate to the inadequate representation of fast physical processes, such as convection (Holloway et al. 2012), the transition from shallow to deep convection that coincides with the gradual moistening of the troposphere prior to the active MJO phase (Del Genio et al. 2012), and the interaction with the upper ocean (Tseng et al. 2015).

The interaction between the MC and the MJO is two way. First, strong forcing provided by the islands of the MC causes variations in the MJO as it passes (Kiladis et al. 2005). Second, the MJO influences local climate through the modulation of both cloud and precipitation characteristics (Chen and Houze 1997). Rauniyar and Walsh (2011), Oh et al. (2012), Peatman et al. (2014), and Moron et al. (2015) demonstrate that precipitation is enhanced over the islands of the MC and suppressed over the surrounding seas prior to the arrival of the MJO. Conversely, toward the late stages of the active MJO, precipitation anomalies over the islands become negative in advance of that over the oceans. Hence, the MJO progression through the MC is not one of smooth eastward propagation. This is important for forecasting regional precipitation and also for global circulation, as the response to a smoothly eastward-propagating heat source will be different to the response to a more complex propagating heat source.

Peatman et al. (2014) hypothesize that this behavior is a consequence of the interplay between the large-scale circulation and mesoscale circulations forced by the islands of the MC. The large-scale circulation and moisture convergence changes preceding the arrival of the MJO, which are forced by large-scale equatorial wave dynamics (e.g., Hendon and Salby 1994; Maloney and Hartmann 1998; Matthews 2000), increase the moisture availability before the active phase of the MJO sets in over the MC. Peatman et al. (2014) suggest that the reason rainfall is enhanced at this time over the land but not the ocean is because solar insolation remains high ahead of the active MJO, which maintains the high land–sea temperature contrast that drives the main rain-producing mechanism in this region. As a consequence of their coarse horizontal resolution, GCM simulations and reanalysis products are unable to adequately reproduce these mesoscale circulations. Furthermore, the necessary observations of these mesoscale circulations are very limited in this region, and thus Peatman et al. (2014) were unable to fully support their hypothesis.

With recent increases in computing power, we now have the ability to run regional climate model (RCM) simulations 1) with horizontal grid spacings that are small enough to capture at least some of the detail of the complex regional coastlines and topography, 2) with horizontal grid spacings that are small enough to allow the convective parameterization to be switched off and the convection to develop explicitly, and 3) for sufficiently long periods that modes of intraseasonal variability can be captured. The higher horizontal resolution allows the representation of mesoscale processes such as the land–sea breeze (Birch et al. 2015). Convection-permitting configurations respond more realistically to surface triggers over land (Birch et al. 2014a), produce a more realistic phase timing of the diurnal cycle of rainfall (Love et al. 2011) and rainfall distribution (Holloway et al. 2012), and in some cases exhibit a better eastward propagation of the active convection envelope of the MJO (Holloway et al. 2013).

Two 10-yr RCM simulations with grid spacings at 12 km (parameterized convection) and 4.5 km (convection permitting) are utilized in this study to 1) understand the reasons for the land–ocean contrasts in MC rainfall by MJO phase and 2) understand the impact of high horizontal grid resolution and the representation of convection on the MJO in regional climate models. A novel aspect of this study is the length of the high-resolution regional climate model simulations, which allows an investigation of the interplay between the large-scale convective environment and mesoscale circulations (viz., land–sea breezes) within a mode of intraseasonal variability. Section 2 outlines the model simulations and observations used in this study. Section 3 evaluates the performance of the RCMs relative to observations and then uses a combination of model and observational data to demonstrate how large-scale and mesoscale components of the convective environment vary by MJO phase. Section 4 synthesizes the results to determine whether sufficient evidence exists to support the Peatman et al. (2014) hypothesis. Conclusions follow in section 5.

2. Data and methodology

a. RCM configurations

Two RCM configurations of the Met Office Unified Model (MetUM), which were developed through the Singapore Variable-Resolution Model (SINGV) numerical weather prediction project, are used in this study. Both employ the Even Newer Dynamics for General Atmospheric Modelling of the Environment (ENDGame) dynamical core (Wood et al. 2014) and parameterize key processes such as mixed-phase microphysics (Wilson and Ballard 1999), clouds (Wilson

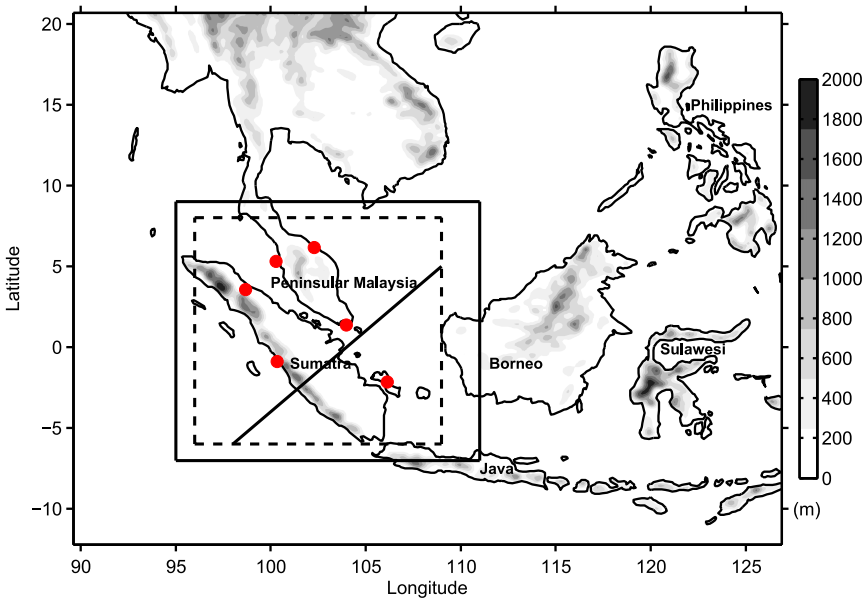

FIG. 1. Orography height (shading) and the RCM domains; the edge of the plot marks the limit of the RCM12 domain, the solid black box marks the limit of the RCM4.5 domain, and the dashed black box the limit of the analysis area. The red dots indicate the locations of the radiosonde observations used in the analysis, and the major regions are labeled. (The diagonal black line marks the transect used in Fig. 4.).

et al. 2008a,b), and the surface (Essery et al. 2001; Best et al. 2011). The first RCM configuration was run with 12-km horizontal grid spacing over a domain of 340 × 300 grid boxes, covering 12°S–21°N, 90°–127°E (RCM12; Fig. 1). RCM12 is similar to the standard MetUM Global Atmosphere 3.0 (GA3.0) configuration (Walters et al. 2014; Mizielinski et al. 2014), parameterizing cumulus convection (Gregory and Rowntree 1990) and employing the standard MetUM one-dimensional (1D) planetary boundary layer (PBL) scheme (Lock et al. 2000).

The second RCM configuration was run with 4.5-km horizontal grid spacing over a domain of 390 × 390 grid boxes, covering 7°S–9°N, 95°–110°E (RCM4.5; Fig. 1). Unlike RCM12, RCM4.5 is a convection-permitting (CP) simulation, such that mid- and deep-level convection is not parameterized and is allowed to develop explicitly. The shallow convection parameterization, however, remains switched on to help represent the effects of convection that remain unresolved at these scales. RCM4.5 also employs the gray-zone blended PBL scheme (Boutle et al. 2014), which dynamically combines the standard MetUM 1D PBL scheme with a 3D Smagorinsky turbulence scheme [see section 2 of Pearson et al. (2014) for further details], depending on how well resolved the turbulent scales are predicted to be at a given horizontal grid spacing. A revised warm rain microphysics scheme (Boutle et al. 2014) is also utilized in the RCM4.5 configuration.

A grid spacing of 4.5 km is reasonably coarse for representing convective processes without the help of a convective parameterization scheme, although this choice of resolution can be justified. This grid spacing was chosen through a necessary compromise involving the computational expense associated with model resolution, domain size, and length of simulation. Previous work through the U.K.-based Cascade project (Pearson et al. 2014) has shown that CP simulations at 1.5, 4, and 12 km produce similar results, as assessed through metrics such as the diurnal cycle, mean rainfall, storm organization and propagation, and the sensitivity to triggers such as low-level convergence (Holloway et al. 2012; Pearson et al. 2014; Birch et al. 2014b). The CP simulations at these grid spacings generally outperformed those simulations with a convective parameterization, and differences between the CP and parameterized convection simulations were much larger than those between the CP simulations at different resolutions. Comparisons between RCM4.5 and a similar RCM with 1.5-km grid spacing (RCM1.5; over a much smaller domain, which is not appropriate for this study) have also been performed (Webster et al. 2015). This work demonstrates that the differences between RCM4.5 and RCM1.5 were much smaller than the differences between RCM4.5 and RCM12,

indicating that while not perfect, 4.5-km grid spacing is a reasonable choice.

Both RCM12 and RCM4.5 are run under present-day climate for 10 years between June 2000 and June 2010, with an additional 7 months of simulation prior to June 2000 to allow for spinup. RCM12 receives its lateral boundary conditions (LBCs) from ERA-Interim data (hereafter ERAI; Dee et al. 2011; ECMWF 2015) every 6 h, and RCM4.5 is forced every hour by LBCs derived from RCM12. Both simulations are free running other than the forcing provided by the LBCs. RCM12 (RCM4.5) has 63 (80) vertical levels with 3 (5) in the lowest 100 m and 16 (20) in the lowest 2 km. The time steps of RCM12 and RCM4.5 are 180 and 100 s, respectively.

SSTs were prescribed daily in both configurations from the Operational Sea Surface Temperature and Sea Ice Analysis (OSTIA; Donlon et al. 2012) dataset, which has a native resolution of 1/20°. Soil moisture was initialized using the soil moisture of the respective driving model at the initialization time (i.e., ERAI for RCM12 and RCM12 for RCM4.5). Surface vegetation was derived from the International Geosphere–Biosphere Programme (IGBP) 1-km resolution dataset.

b. Observations

The Tropical Rainfall Measuring Mission (TRMM) 3G01 brightness temperature and 3B42 rainfall dataset are used in this study (Huffman et al. 2007; NASA 2015). The 3B42 product combines precipitation estimates from multiple satellites and land surface precipitation from rain gauges and is available at 3-hourly temporal resolution and 0.25° horizontal resolution. It is known to have particular problems over steep topography, where biases have a strong dependence on elevation (Romilly and Gebremichael 2011). In particular, over the steep and high topography of Papua, New Guinea, at the heart of the MC, TRMM rainfall consistently underestimates station rainfall by a factor of 2, both in the climatological mean and in its MJO anomalies (Matthews et al. 2013). The TRMM and station rainfall agree over the low-lying coastal plains. In addition, the satellite-derived precipitation maximum corresponds with the maximum in deep convective precipitation, which may be delayed by one or two hours relative to surface observations that include earlier rainfall from shallower clouds (Dai et al. 2007). These biases should be taken into account during comparisons with model rainfall, although in this study, the absolute amounts of rainfall and the precise phase of the diurnal cycle are of secondary importance to their anomalies by MJO phase.

Radiosonde observations from the locations marked by the red dots in Fig. 1 are used to compare with the RCM simulations (NOAA 2015). Other stations do exist within the model domains, but these locations were selected because of their near-complete data record over the years 2000–10. Although some of the stations release two sondes per day [0000 and 1200 UTC or 0700 and 1900 local standard time (LST) defined as UTC + 7 h], only the 0000 UTC launches are used here because the data coverage is more complete and convection over land is at a minimum at this time, which allows an illustration of the large-scale conditions without the complicating presence of convective systems.

TABLE 1. Number of days in each MJO phase used in this study.

Phase	Number of days
1	42
2	70
3	92
4	60
5	80
6	83
7	113
8	74
Total	614

c. MJO phase identification

The model and observational data are averaged over each MJO phase, as derived by Wheeler and Hendon (2004) using outgoing longwave radiation (OLR) satellite observations and wind data from NCEP analyses. This study analyzes model and observational data for the 2000–10 boreal winter months of December–February (DJF) only, since this is when the MJO tends to be strongest. The averages exclude days on which the MJO was weak; that is, when the amplitude[1] is defined as

$$\sqrt{(\mathrm{RMM1})^2 + (\mathrm{RMM2})^2} < 1, \qquad (1)$$

which leaves 614 days out of a possible 902 days available for the analysis, with between 42 and 113 days in each of the 8 standard MJO phases (Table 1). Note that the MJO phases were derived from the observations only. As the (limited area) model was forced by observed lateral boundary conditions and observed SSTs (with their embedded MJO signals), the underlying assumption is that the model MJO phase is the same as the observations on any given day. This assumption is tested in section 3 through comparisons between observed and model rainfall, winds, humidity, and temperature.

[1] The standard definition of the MJO in Wheeler and Hendon (2004) uses the real-time multivariate MJO indices (RMM1 and RMM2) in a two-dimensional phase space, which is split arbitrarily into 8 MJO phases (i.e., each lasting for 1/8 of an MJO cycle) for convenience.

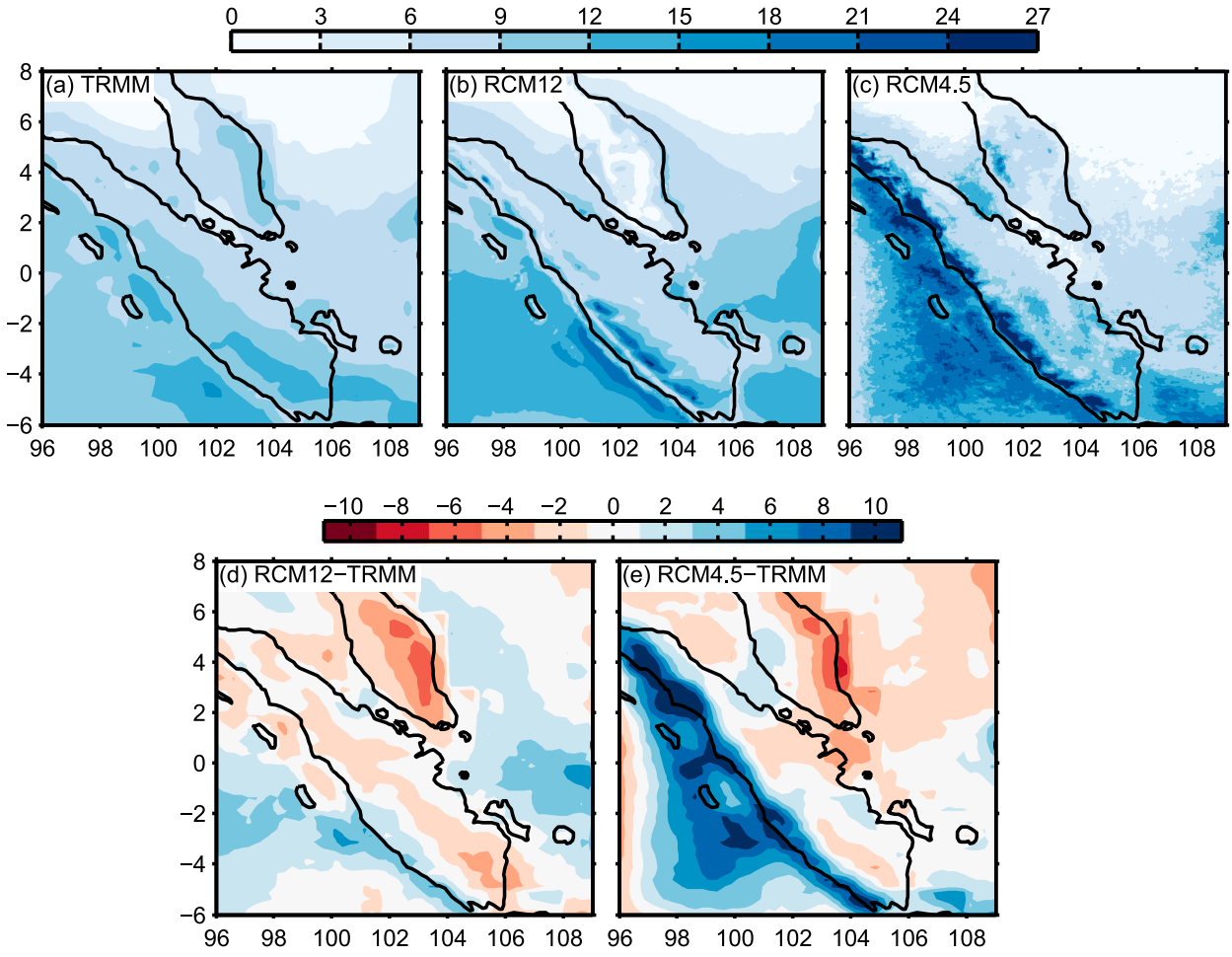

FIG. 2. Mean DJF rainfall over 2000–10 (mm day^{-1}) from (a) TRMM 3B42, (b) RCM12, and (c) RCM4.5 and precipitation bias, and shown are the differences (d) RCM12 minus TRMM and (e) RCM4.5 minus TRMM. The RCM data are interpolated onto the TRMM grid in (d) and (e).

Where anomalies by MJO phase are presented (see Figs. 5, 8, and 9), the anomalies are computed as differences relative to the observations' or RCM's own climatology, where in this sense the climatology is equal to mean in MJO phase x minus mean over all days with amplitude >1. The climatology is computed using only days with a strong MJO (amplitude >1), rather than all days, so that the sum of the eight anomalies is equal to zero. Using all days makes negligible difference to the results.

3. Results

a. *Evaluation of model rainfall*

In this section the two RCMs are evaluated against TRMM observations. The observed and RCM mean DJF rainfall for 2000–10 is shown in Figs. 2a–c for the subdomain 6°S–8°N, 96°–109°E (Fig. 1, dashed box). This subdomain is also used as the averaging area in subsequent figures. In TRMM and the two RCMs rain rates are highest toward the south of the domain, as expected for the boreal winter monsoon. Localized peaks in rainfall occur over the high topography in western Sumatra, off the coasts of western and southern Sumatra, and along the east coast of peninsular Malaysia in both TRMM and the RCMs. The minimum in rainfall observed in TRMM along the west coast of Sumatra is also reproduced by both RCMs.

The difference between RCM and observed rainfall for all days in DJF 2000–10 is shown in Figs. 2d,e. RCM12 is drier than TRMM by 1–6 mm day^{-1} over most of the land within the domain. Over southwestern Sumatra, oceanic regions west of Sumatra and in the Java Sea, and to the east of Sumatra the model is wetter than TRMM by 1–6 mm day^{-1}. RCM4.5 is up to 8 mm day^{-1} wetter than TRMM along the west coast of Sumatra and extending

out over the coastal ocean to 97°E. Both models fail to capture the distinct winter monsoon rainfall feature observed over the eastern Malay Peninsula. RCM4.5 in particular has high rainfall rates over the mountains in western Sumatra and over the ocean to the southwest. This bias does, however, change sign to a dry bias right at the edge of the averaging box (96°–97°E), which is likely a consequence of the proximity to the edge of the domain at 95°E. While there are known issues with TRMM in the MC region, it is unlikely that the model–observation differences are solely due to TRMM uncertainties. Wet biases from high rainfall rates in CP configurations of the MetUM, especially over high orography, are a known issue in a number of regions of the world (Birch et al. 2014a; Kendon et al. 2012) and also in other CP models (e.g., Hassim et al. 2016), and this bias is the subject of ongoing research at the Met Office.

The mean amplitude and phase of the diurnal precipitation maximum, computed as the first harmonic of the diurnal cycle, are shown in Fig. 3. In the TRMM observations the diurnal amplitude of rainfall r_d is largest (8–18 mm day^{-1}) over the western side of Sumatra and over the coastal seas to the west of Sumatra. RCM4.5 reproduces the spatial variations in the observed amplitude better than RCM12, although there are differences in the magnitude of up to 8 mm day^{-1} in RCM4.5, which is a consequence of the differences in rainfall rates shown in Fig. 2c. RCM4.5 is, however, in better agreement with the observations over the ocean, where the amplitude is $<$4 mm day^{-1} and rainfall rates are $<$6 mm day^{-1}. In RCM12 the magnitude of the diurnal amplitude is higher than in TRMM along the west coast of Sumatra, and there is also no southwest–northeast gradient in amplitude across Sumatra.

Regions where the amplitude is less than 4 mm day^{-1} are set to white in the phase plots (Figs. 3d–f). In the observations rainfall appears first just inland of the coast between 1400 and 2000 LST (light brown and yellow colors). It then peaks inland between 2000 and 0000 LST (deep red and pink colors), before propagating offshore and peaking over the coastal ocean between 0000 and 0800 LST (purple and blue colors). The rainfall finally peaks over oceanic regions that are remote from the coastlines between 0800 and 1000 LST.

The timing of the diurnal peak in rainfall in RCM12 does not agree with the TRMM observations. The rainfall peaks 4–10 h too early over both land (0800–1600 LST) and ocean (2200–0600 LST), which is a well-known bias in models where convection is parameterized (Dai 2006; Birch et al. 2014a, 2015). There is evidence of the propagation of storms off the west coast of Sumatra, although the diurnal timing is too early. The diurnal cycle in RCM4.5 is much more similar to TRMM, although the diurnal timing over land is 2–3 h later than in the observations. This 2–3-h difference in timing could be due to uncertainties in the satellite retrievals (Dai et al. 2007), or it could be a consequence of the relatively coarse grid spacing for a CP model configuration, in which strong convective updrafts are unable to develop until slightly later in the day.

The diurnal cycle of the storms' offshore propagation is a key component of convection in the MC region (Qian 2008; Mori et al. 2004). Figure 4 presents Hovmöller plots of the mean diurnal cycle of precipitation along the diagonal transect marked in Fig. 1. In TRMM (Fig. 4a) the precipitation first appears over the mountains along the west coast of Sumatra between 1200 and 1500 LST and moves inland until around 2100 LST. At about 1800 LST precipitation begins to propagate toward the southwest, reaching beyond the analysis domain boundary at 98°E. Weaker propagation also occurs off the northeast coast but this begins later in the day, at 2100 or 0000 LST. Precipitation appears too early over the land in RCM12 (as discussed in relation to Fig. 3), and the precipitation begins over the flat land in the middle of the island; then the peak rainfall moves toward both coasts, rather than beginning along the west coast as seen in TRMM (Fig. 4b). RCM12 does, however, produce a propagating signal off the southwest coast. A propagating signal is not apparent off the northeast coast; rather, it rains on average more than 10 mm hr^{-1} between 1500 and 0900 LST. In RCM4.5 the timing and location of the appearance of rainfall over Sumatra is in agreement with that in TRMM, although the rainfall rates are too high over land, and there is a wet bias over the ocean in the signal propagating toward the southwest (Fig. 4c). As with RCM12, there is no offshore propagating signal toward the northeast in the early morning between 0000 and 0900 LST.

b. *Behavior of key model diagnostics by MJO phase*

In this section RCM rainfall and OLR anomalies by MJO phase are evaluated against TRMM observations. The large-scale MJO develops over the Indian Ocean (phases 1 and 2), moves eastward over the MC (phases 3 and 4), and then moves over the western Pacific (phases 5–8). However, this simple eastward progression is more complicated over the MC. The TRMM observations shown in the left-hand column of Fig. 5 illustrate the results of Peatman et al. (2014), who showed that in the MC region, the peak in rainfall over land does not occur in the same MJO phase as that over the ocean (see Fig. 5 of Peatman et al. 2014). Over the western MC in phase 1, precipitation is suppressed over the ocean but is wetter than average along the west coast of the islands. In phases 2 and 3 the large-scale active envelope of MJO

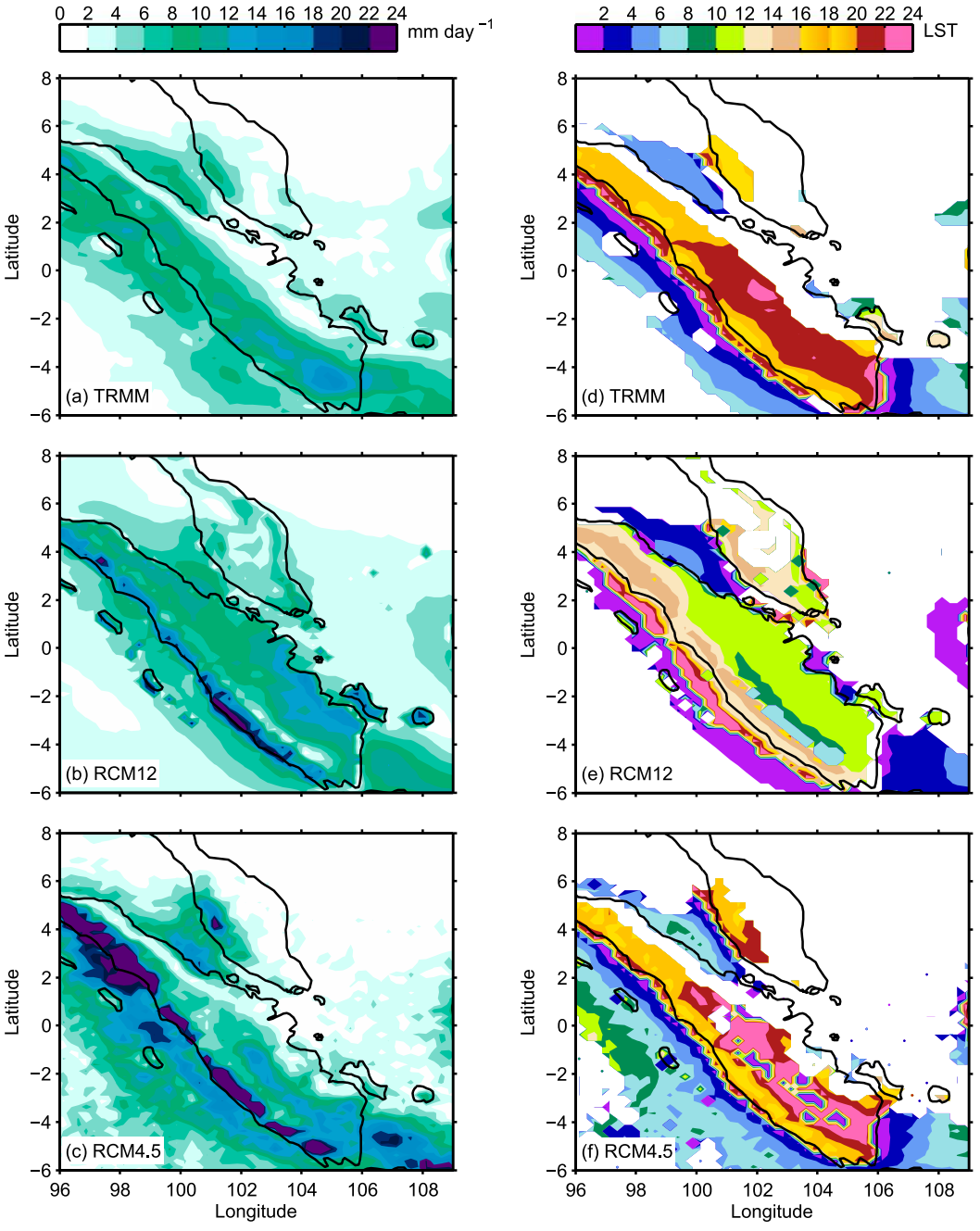

FIG. 3. (a)–(c) The amplitude and (d)–(f) LST of the phase of the precipitation maximum of the first harmonic of the diurnal cycle r_d for DJF precipitation over 2000–10 for TRMM, RCM12, and RCM4.5. The RCM data are interpolated onto the TRMM grid, and regions where the amplitude is less than 4 mm day^{-1} are set to white in the phase plots.

convection moves over the western MC and rainfall is higher than average over both land and ocean. In phases 4 and 5 the large-scale active envelope of convection remains over the western MC and strong negative rainfall anomalies persist over the ocean, but there are generally dry anomalies over land. Phases 6–8 are the suppressed phases of the MJO over the western MC and rainfall is lower than average over both land and ocean.

Both RCM12 and RCM4.5 reproduce most of the spatial differences in rainfall anomaly by MJO phase. RCM12 reproduces a clear land–ocean contrast in phases

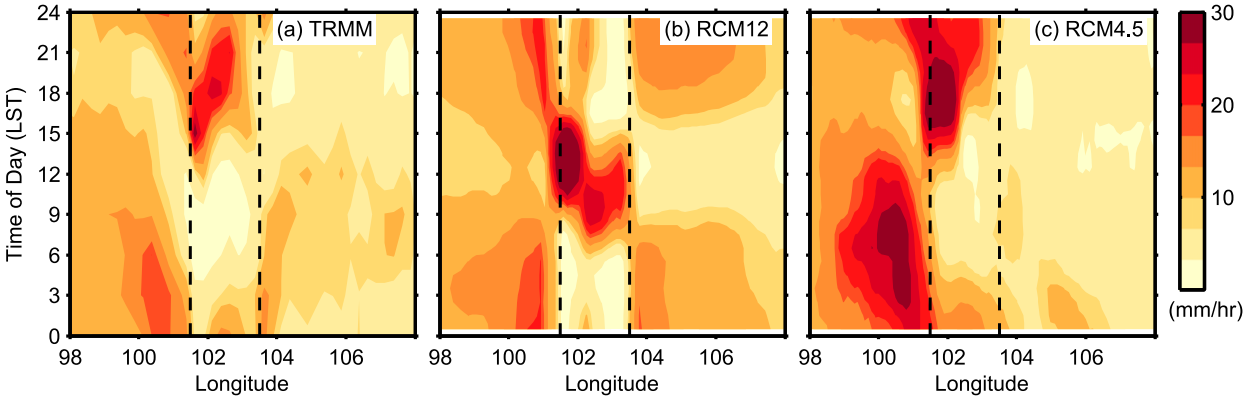

FIG. 4. Mean diurnal cycle of DJF 2000–10 precipitation (mm h^{-1}) along the diagonal transect marked in Fig. 1 for (a) TRMM, (b) RCM12, and (c) RCM4.5. The dashed black lines mark the coastlines of Sumatra.

1, 4, and 5 and dry anomalies in phases 6–8, although the magnitudes of the anomalies are smaller than in the observations. RCM4.5 also reproduces the land–ocean contrast trend well, with a clear difference in rainfall between the active and suppressed phases, although localized patches of wet anomaly persist through the suppressed phases. There is generally good agreement between the RCMs and the TRMM observations, showing that the RCMs are correctly reproducing the timing of the active MJO passage, which, given that the RCM domains are relatively small and that they are constrained by ERAI data at the boundaries, is an anticipated but not certain result a priori.

A more quantitative comparison of the land–ocean contrasts is shown in Fig. 6. The mean brightness temperature from TRMM T_b, which indicates the arrival of the active MJO envelope by the presence of extensive, high cloud, peaks in phase 3 over both land and sea (Fig. 6a). In agreement with Peatman et al. (2014), the solid red and blue lines show a clear phase separation in TRMM mean rainfall between land and ocean, with a broad peak over land in phases 1, 2, and 3 and a later peak over the ocean in phase 3. The change in amplitude of the diurnal cycle over land and ocean r_d (Fig. 6, dashed red and blue lines) is almost in phase with the mean rainfall rates (i.e., largest when the precipitation rate is largest).

Brightness temperature is not available as a model diagnostic, so OLR is plotted instead for the two RCMs. RCM12 and RCM4.5 both reproduce the change in cloudiness (OLR) by MJO phase and the slightly higher cloud cover over land in most phases. Both models have a broad peak over phases 3–5, and RCM4.5 slightly overestimates cloud in phase 5 (Figs. 6b,c). For the most part RCM12 and RCM4.5 reproduce the land–ocean phase difference in the mean rainfall rates. The peak in rainfall over land occurs in phases 2 and 3 in both model configurations; the variation in the diurnal amplitude of rainfall over land is in phase with this, but the change in rainfall rates by phase is too small. The model performance over the ocean is, however, less successful. The model rainfall rates do not vary as much by MJO phase as in the observations, and the peak in rainfall is in phases 3–5 in RCM12 and in phase 5 in RCM4.5, compared to phase 3 in the observations. Unlike over land, the change in the amplitude of the diurnal cycle of rainfall over ocean does not vary enough by MJO phase in the two RCMs and the amplitude over the ocean in RCM4.5 is too large (as also shown in Fig. 3e). Nevertheless, both model configurations have reproduced the observed phase shift in the variation in oceanic rainfall by MJO phase compared to the variation in land-based rainfall by MJO phase; that is, high-rainfall MJO phases over land occur before the high-rainfall MJO phases over the ocean.

c. *Large-scale processes by MJO phase*

In this section the ability of the RCMs to represent variations of key aspects of the large-scale circulation are evaluated against observations and the ERAI data that were used to force the boundaries of the RCMs. A combination of the observations and RCMs are then used to understand how domainwide indicators of the convective environment vary by MJO phase. Figure 7 shows mean vertical profiles of the westerly component of the wind U by MJO phase, averaged over the six radiosonde stations marked in Fig. 1. Domain-mean U profiles for ERAI and the RCMs are very similar to the means over the six radiosonde stations (not shown), indicating that the six stations are representative of domain-mean conditions. The observations show that, on average, easterly winds persist over the entire column in the wet phases (2 and 3) and those immediately preceding them (8 and 1) and become weakly easterly or

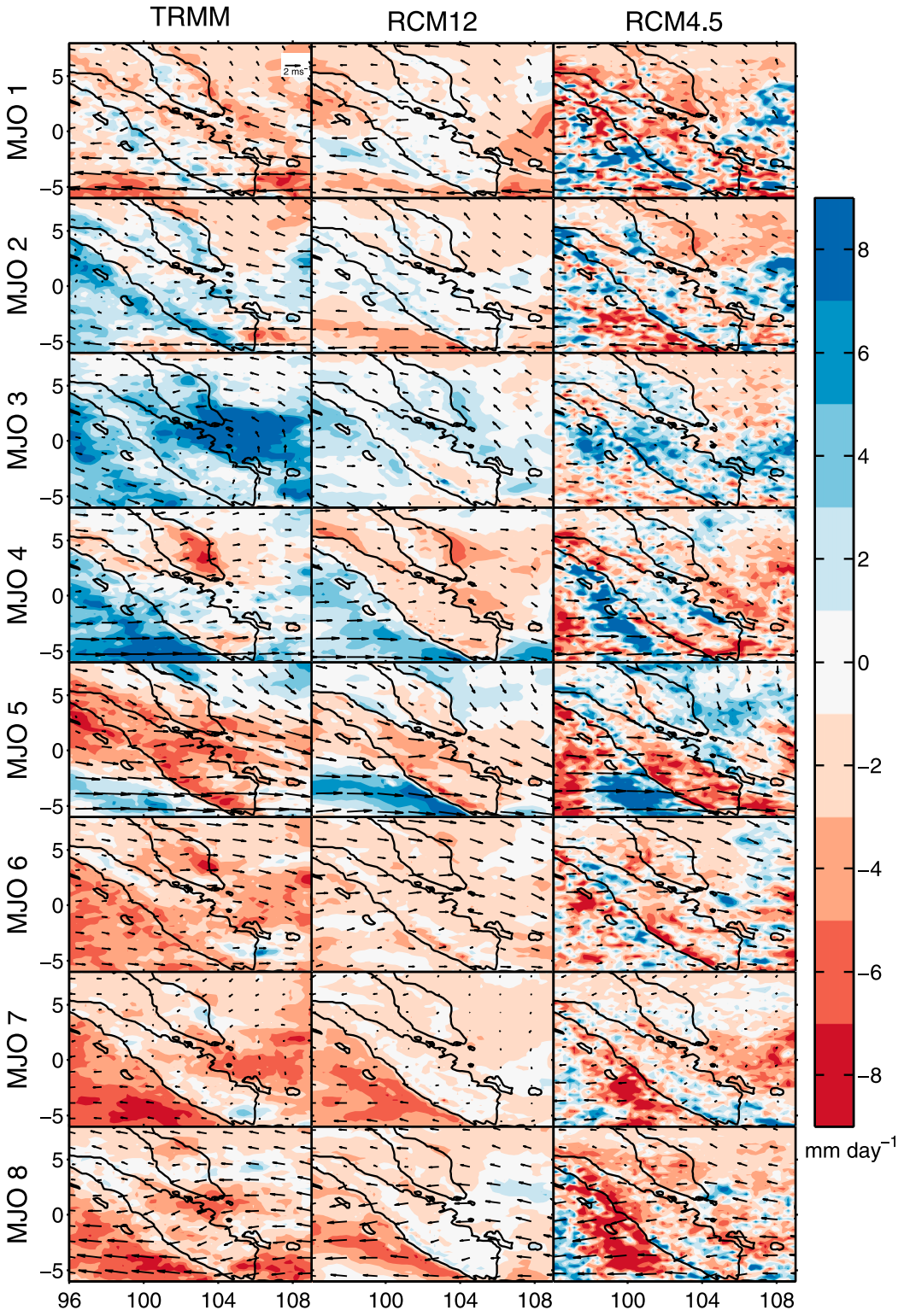

FIG. 5. Precipitation and 850-hPa wind vector anomalies (m s^{-1}) by (top)–(bottom) MJO phase for (left) TRMM and ERAI, (center) RCM12, and (right) RCM4.5. The RCM data are interpolated onto the TRMM grid. The scale of the arrows is illustrated in the corner of the top-left panel.

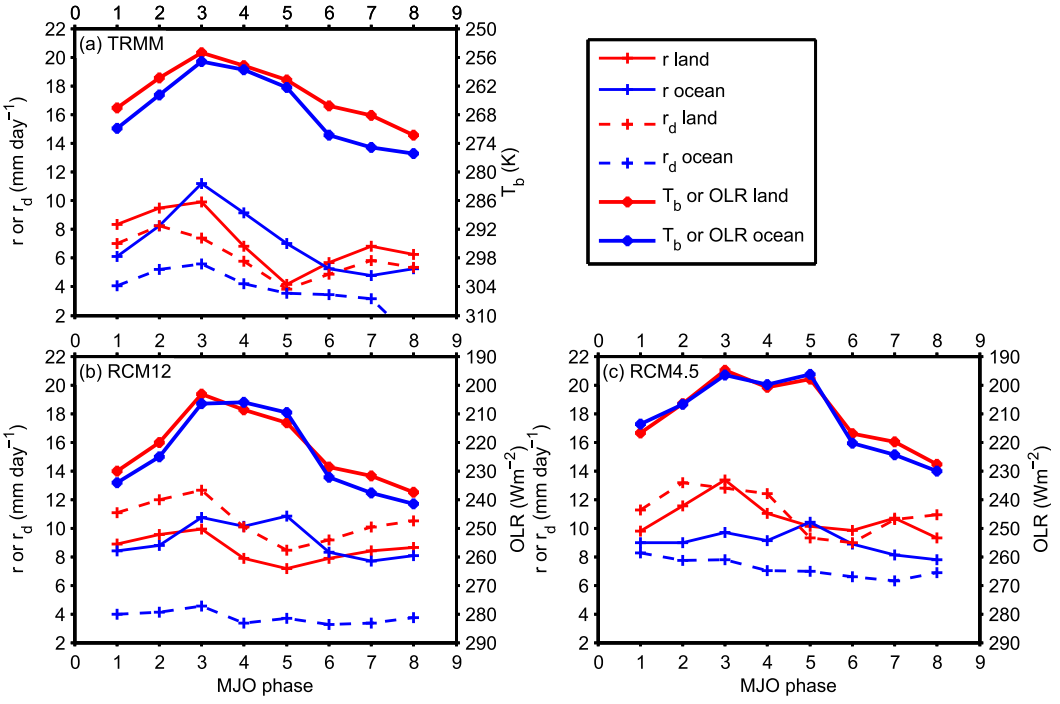

FIG. 6. Brightness temperature T_b or OLR, mean precipitation r, and the amplitude of the first harmonic of r_d by MJO phase, averaged over land and ocean for (a) TRMM, (b) RCM12, and (c) RCM4.5. The averaging domain is illustrated by the dashed black box in Fig. 1.

westerly toward the end of the wet period (phase 5) and into the drier phases (6 and 7). The largest differences are at midlevels (800–500 hPa), which is consistent with equatorial wave dynamics theory (Matthews 2000). The ERAI data and the two RCMs behave in a similar way to the observations, except that the westerly midlevel winds in phases 5 and 6 are weaker than observed. The low-level winds (1000–800 hPa) are reproduced better in RCM4.5 than RCM12, which may be due to the greater number of vertical levels in RCM4.5 or the use of the 3D diffusion scheme. Since the RCMs receive their large-scale forcing from ERAI, the RCM–observation difference is likely explained by the ERAI–observation difference.

The spatial variability of the 850-hPa wind anomaly vectors is shown in Fig. 5 for ERAI and the two RCMs. In phases 8, 1, and 2 there is a large southerly or southeasterly anomaly over the ocean in the east of the domain and an easterly anomaly in the west of the domain. In phase 3 the strong southerly anomaly persists in the east of the domain but a northwesterly anomaly develops in the west, which persists through phases 5 and 6. Apart from a few exceptions, such as in the northeastern part of the domain in phase 3, both RCMs reproduce most of the main features of these wind anomalies both in terms of spatial variability with the domain and in temporal change by MJO phase, which is an anticipated result, given that ERAI drives the large-scale conditions in the RCMs.

The variation in the ability of the large-scale environment to develop and sustain convection by MJO phase is now considered. The equivalent potential temperature θ_e is a measure of both temperature and humidity in the vertical profile and therefore is an indictor of convective potential. The saturated equivalent potential temperature θ_{es} is the potential temperature the air would have if it were saturated and thus enables the temperature of the profiles to be compared relative to ascending saturated parcels. The anomalies of θ_e and θ_{es} by MJO phase from the radiosonde observations, ERAI, and the two RCMs are shown in Figs. 8 and 9. The model anomalies are only negligibly different if averaged over the entire averaging domain or over the land and ocean points separately (not shown), which gives confidence that Figs. 8 and 9 are representative of changes to the domainwide environment by MJO phase. There is broad agreement between the observations, ERAI, and two RCMs, although the anomalies by MJO phase for θ_e are larger in the observations than in ERAI or the two RCMs. Also necessary for this analysis is the domainwide (as indicated by the black dashed box in Fig. 1) column-integrated moisture flux convergence

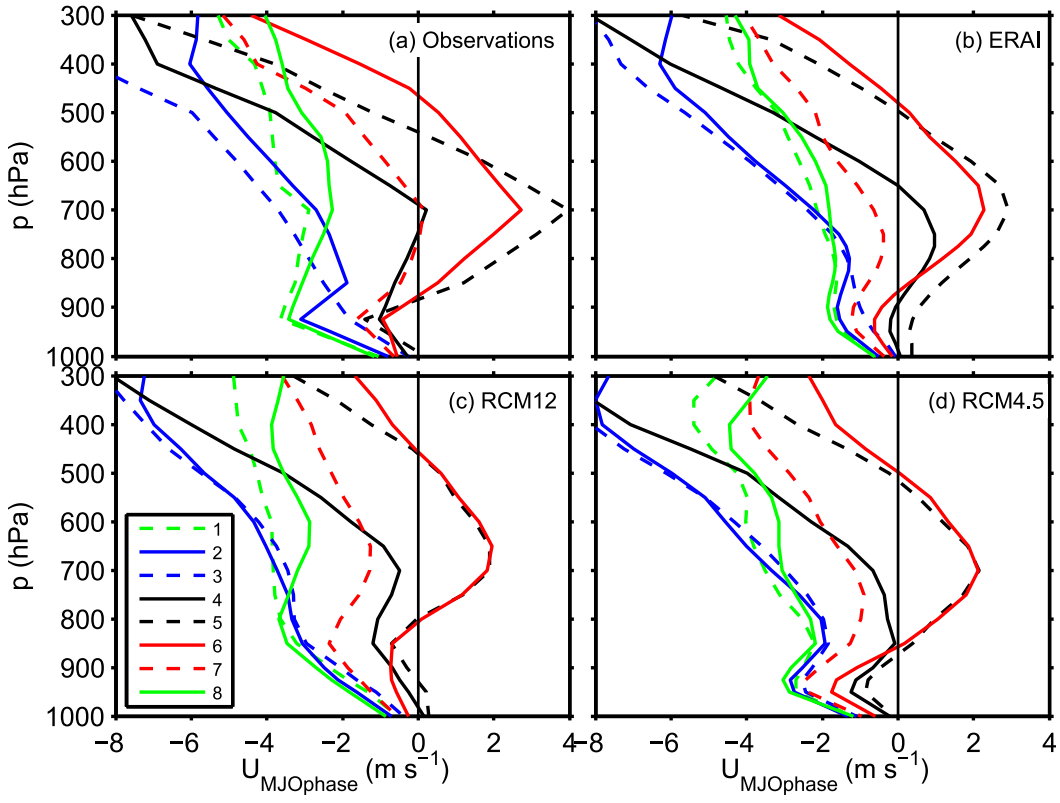

FIG. 7. Profiles of the mean U component of wind speed at 0000 UTC (0700 LST), averaged over the six radiosonde stations locations marked in Fig. 1 for (a) observations, (b) ERAI, (c) RCM12, and (d) RCM4.5.

(MFC) by MJO phase (Fig. 10). It is computed from ERAI rather than the RCM data because the RCMs are forced at the boundary by ERAI, and previous plots have shown that the change in winds, θ_e, and θ_{es} by MJO phase are very similar in ERAI.

In phase 1 the active envelope of MJO convection is to the west of the MC, moisture flux convergence is small but positive, and the θ_e anomaly is small. Moisture flux convergence peaks in phase 2 and coincides in time with a positive θ_e anomaly, which indicates a warm and moist profile, which is favorable to convection. The θ_e anomaly remains high in phase 3 because the atmospheric moisture, forced by moisture convergence, takes time to build. A strong positive θ_{es} anomaly below 800 hPa and a negative θ_{es} anomaly above 800 hPa occur in phases 3 and 4, indicating an unstable profile with warm and humid air in the lower atmosphere and cool air above, which is also favorable for convection. In phase 4 the magnitude of moisture flux convergence has greatly decreased and the θ_e anomaly has changed to negative at midlevels, although it remains near zero or positive near the surface. The highly unstable profile in phase 4 maintains the rainfall in this phase, even though the moisture availability has decreased.

In phases 5–7, during the suppressed MJO phases, moisture flux convergence is negative (moisture flux divergence) and the θ_e anomaly becomes negative, indicating a drier environment that is unfavorable for convection. Additionally, θ_{es} is low below 800 hPa and high above 800 hPa, suggesting a stable profile, which is also unfavorable for convection. Phase 8 shows signs of the next active MJO phase; the moisture flux convergence remains negative, but θ_e builds to a near-zero anomaly and the θ_{es} profile begins to warm.

In summary, this section has shown that there are distinct variations in the large-scale potential for convection by MJO phase in the two RCMs. Heat, moisture, and instability build gradually between phases 6, 7, 8, 1, 2, and 3 and then decrease more rapidly between phases 3, 4, 5, and 6. The next section will investigate how the afternoon onshore flow and surface fluxes vary by MJO phase. The interaction between the mesoscale and domainwide atmospheric state will be discussed in section 4.

d. *Mesoscale processes by MJO phase*

Low-level convergence produced by sea breezes propagating inland from the coast is known to be a major mechanism for convection initiation in the MC

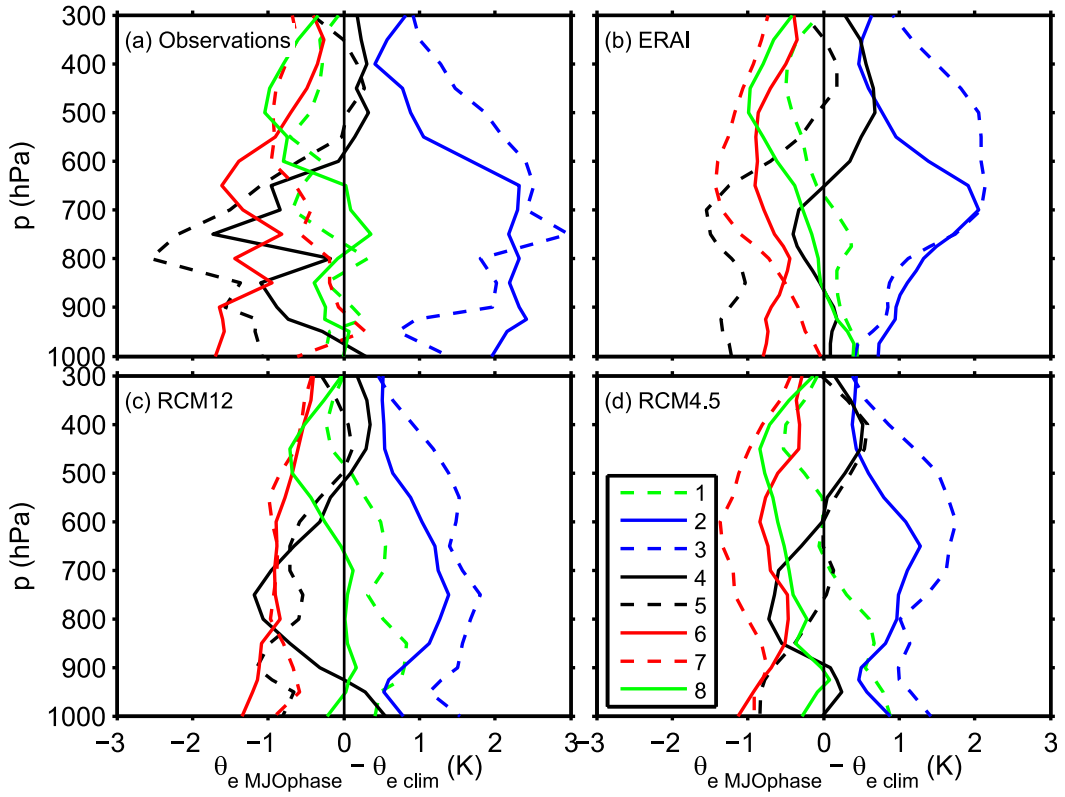

FIG. 8. Anomaly profiles of θ_e at 0000 UTC (0700 LST) averaged over the six radiosonde stations locations marked in Fig. 1 for (a) observations, (b) ERAI, (c) RCM12, and (d) RCM4.5.

region (Qian 2008). It is hypothesized by Peatman et al. (2014) that a weaker sea breeze, caused by reduced solar insolation, is one of the reasons why the rainfall rate decreases over land in phase 4, even though the region still lies in the large-scale envelope of MJO convection.

Figures 11a,b show the domain-mean downward surface shortwave radiation flux SW_{dn} over land and sea by MJO phase in the two RCM simulations. The variability in SW_{dn} by MJO phase ties in well with the variability in OLR shown in Figs. 6b,c. The low OLR values (extensive and/or high cloud tops) in phases 3–5 coincide with the lowest SW_{dn} fluxes, whereas the highest fluxes occur in phases 8 and 1 when OLR is at its maximum. The magnitude of the SW_{dn} flux is between 5 and 20 W m^{-2} lower over land compared with the ocean, which is associated with the lower OLR over land. The mean SW_{dn} flux is also approximately 40 W m^{-2} higher in RCM12 compared to RCM4.5. Stein et al. (2015) used *CloudSat* observations to evaluate various convection-permitting and convection-parameterized configurations of the MetUM and found that the representation of vertical distribution and occurrence of cloud improves when the horizontal grid spacing is reduced from 12 to 4 km and when the convection parameterization is switched off. It is therefore likely that RCM4.5 performs better than RCM12 in terms of cloud and surface radiation, but it is not possible to say from the current results alone. The absolute differences in SW_{dn} in RCM12 and RCM4.5 are, however, of secondary importance in this study compared to the relative changes by MJO phase, which are very similar in both RCMs.

Sea breezes form as a response to pressure gradients set up by land and sea surface temperature differences. The temperature difference between the coastal ocean and coastal low-lying land is computed for both of the RCMs. Ocean grid boxes within 120 km of the coast and land grid boxes within 120 km of the coast that are <500 m above MSL are identified (shown for RCM12 only, blue and orange regions, respectively, in Fig. 11c). The mean difference between the coastal lowland and coastal sea surface temperature at 1400 LST is then computed for both RCMs (Fig. 11d). In all MJO phases the land surface is warmer than the ocean, but this difference is at a minimum in phases 2–5 and at a maximum in phases 7, 8, and 1. This trend is in broad agreement with the trend in SW_{dn} and OLR, which suggests that the increased cloud during the active phase of the MJO reduces the heating of the land surface. The land–ocean temperature difference is higher in RCM4.5

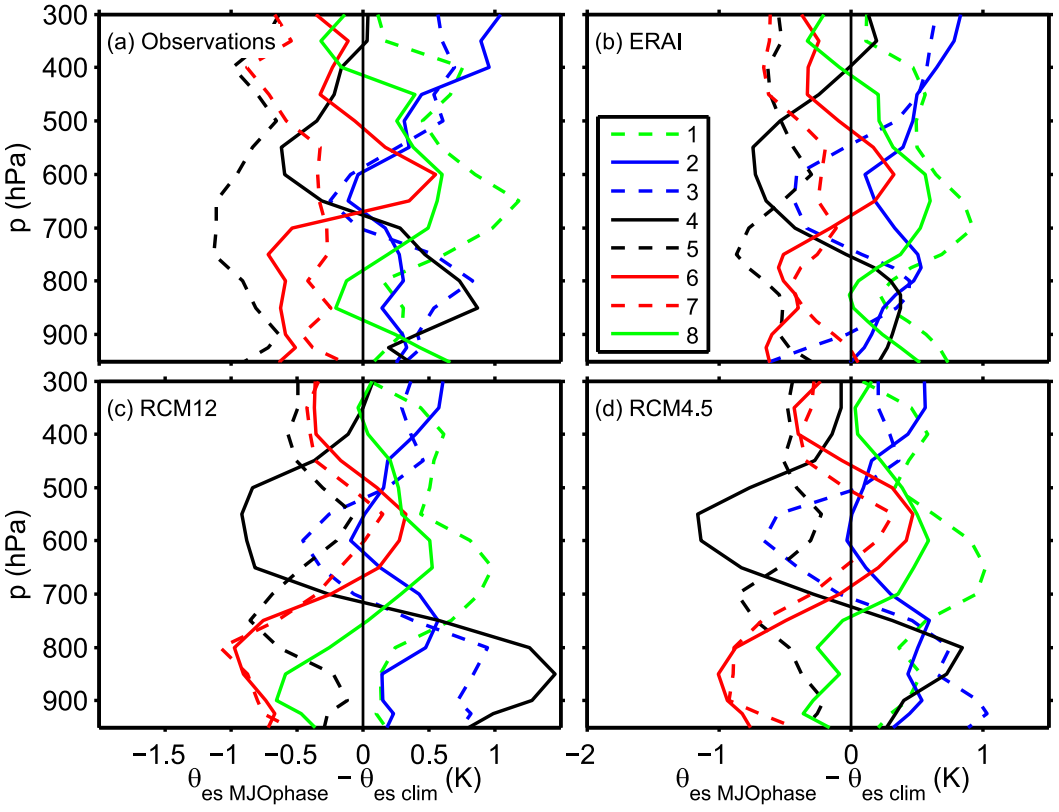

FIG. 9. As in Fig. 8, but for θ_{es}.

compared to RCM12. The SSTs are prescribed from observations and thus the difference must originate from the land surface temperature, which may be a result of the aforementioned differences in cloud or the difference in timing of the diurnal cycle of convection between RCM12 and RCM4.5 (see discussion of Fig. 12 below for more details).

The next step is to link the land–ocean surface temperature differences to the strength of the sea breeze, which is computed following the method of Y. Li et al. (2015, unpublished manuscript). For each coastal grid box (illustrated for RCM12 as black dots in Fig. 11c) the orientation of the coast is identified by its barycenter using the land fraction of the surrounding eight grid boxes:

$$X_B = \mathrm{lsm}(i+1,j) + \mathrm{lsm}(i+1,j+1) + \mathrm{lsm}(i+1,j-1) - \mathrm{lsm}(i-1,j) - \mathrm{lsm}(i-1,j+1) - \mathrm{lsm}(i-1,j-1) \quad (2)$$

and

$$Y_B = \mathrm{lsm}(i-1,j+1) + \mathrm{lsm}(i,j+1) + \mathrm{lsm}(i+1,j+1) - \mathrm{lsm}(i-1,j-1) - \mathrm{lsm}(i,j-1) - \mathrm{lsm}(i+1,j-1), \quad (3)$$

where lsm is the model land–sea mask (land = 1 and sea = 0), and i and j are the indices of a coastal grid box in the meridional and zonal directions, respectively. Only points that have a clear coastal direction are included in the analysis—that is, those that satisfy the following criterion:

$$X_B^2 + Y_B^2 \geq \sqrt{2}, \quad (4)$$

where $\sqrt{2}$ is an arbitrary value, selected through inspection of example coastline configurations. The direction that an onshore wind perpendicular to the coast would have is computed for the coastal points that satisfy the criterion in Eq. (4) using the four-quadrant inverse tangent function:

$$\varphi = \arctan(Y_B/X_B). \quad (5)$$

Here φ is used to rotate the 10-m U and V wind vectors so that a positive model V (northward) wind is an onshore wind perpendicular to the coast. The mean onshore 10-m wind speed at 1400 LST ($WS_{1400LST}$) is computed by taking a mean of the rotated V wind at 1400 LST on all days in each MJO phase. The sea breeze for each MJO phase ($SB_{1400LST}$) is the diurnal anomaly of this value at 1400 LST:

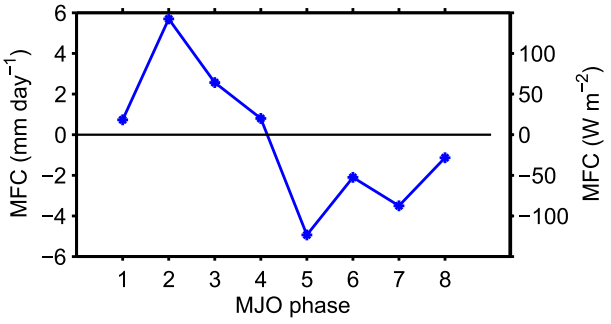

FIG. 10. ERAI column-integrated MFC by MJO phase for the days in Table 1, averaged over the domain marked by the dashed black box in Fig. 1.

$$SB_{1400LST} = WS_{1400LST} - WS_{dailymean}, \quad (6)$$

where $WS_{dailymean}$ is the daily mean onshore wind speed in each MJO phase. Both the total onshore wind speed $WS_{1400LST}$ and its anomaly $SB_{1400LST}$ are presented here (Fig. 11e) because, although quantifying the contribution of the sea breeze is important, it is the total onshore flow rather than the contribution of the sea breeze alone that impacts afternoon inland convergence. Total onshore flow includes the impact of the sea breeze, upslope mountain flow forced by solar heating over the mountains along the coast of Sumatra, and the synoptic-scale circulation. There is a clear change in the strength of the onshore flow ($WS_{1400LST}$) by MJO phase in both RCMs; the flow is weak in phases 3–5 when the land–ocean temperature contrast is small, and the flow is strong in phases 7, 8, and 1 when the land–ocean temperature contrast is large.

The change in the strength of $SB_{1400LST}$ in RCM12 follows the change in the total onshore flow. In RCM4.5 the sea breeze is weaker and the variation by MJO phase is reduced compared to RCM12. On inspection of mean diurnal cycle plots of onshore wind speed by MJO phase (not shown) the magnitudes of the nocturnal wind speeds are on average higher in RCM4.5 compared to RCM12 and are also more variable. This results in larger values of $WS_{dailymean}$ in Eq. (6), which reduces the strength of $SB_{1400LST}$ and, because of the variability, removes the clear signal by MJO phase that is apparent in $WS_{1400LST}$.

Variations in the surface heat fluxes by MJO phase are now considered. Figures 12a,b show the mean land and ocean surface sensible heat Q_h and latent heat Q_e fluxes by MJO phase. Oceanic Q_h (Figs. 12a,b, blue solid line) is small ($<10\,W\,m^{-2}$) and varies only slightly by MJO phase, whereas oceanic Q_e (Figs. 12a, b, blue dashed line) is larger (100 and $135\,W\,m^{-2}$). Both oceanic fluxes are at a maximum in phase 5 when the 10-m wind speed (Figs. 12e,f) is highest and are at a minimum in phases 1 and 2 when the 10-m wind speed is low.

Over land Q_h (Figs. 12a,b, red solid line) minimum values of approximately $20\,W\,m^{-2}$ occur in phase 3 when OLR (Figs. 6b,c), SW_{dn} (Figs. 11a,b), and the land surface temperature (Figs. 12c,d) are at their lowest. The value of Q_h is at a maximum ($\sim 35\,W\,m^{-2}$) in phases 8 and 1 when OLR, SW_{dn}, and the land surface temperature are at their highest. The variation of land-based Q_e (Figs. 12a, b, red dashed line) approximately follows the trend in land-based Q_h, with the highest values occurring in phases 1 and 8. This analysis suggests that the major control on ocean-based Q_h and Q_e is the wind speed (i.e., wind-induced surface heat exchange) and that the major control on land-based Q_h and Q_e is cloud cover, SW_{dn}, and the land surface temperature.

Although the variation by MJO phase of the key variables discussed in this section is similar in the two RCMs, there are some differences in the absolute values of land-based Q_e and land surface temperature (Figs. 12c,d). The land surface temperature is about 0.5 K lower in RCM12 compared with RCM4.5, and land-based Q_e is approximately $125\,W\,m^{-2}$ in RCM12 compared to approximately $80\,W\,m^{-2}$ in RCM4.5. Very similar differences were found over the MC when analyzing standard and CP global climate model simulations with 17-km horizontal grid spacing in Birch et al. (2015). The daily mean land surface temperature in the MC region in DJF in the global simulation with a standard convective parameterization was about 0.5 K cooler than in the CP simulation (Fig. 10a of Birch et al. 2015). The daily mean surface latent heat flux was approximately $125\,W\,m^{-2}$ in the simulation with a standard convective parameterization compared to approximately $85\,W\,m^{-2}$ in the CP simulation (Fig. 10c of Birch et al. 2015). Birch et al. (2015) show that these differences are caused by biases in the timing of the diurnal cycle of rainfall in the simulation with a convective parameterization (as shown for RCM12 in Fig. 3b). The convective parameterization causes the rainfall to peak in the middle of the day, instead of in the later afternoon and early evening, as observed. The early rainfall cools and wets the land surface in the middle of the day, which lowers the daytime land surface temperatures and land-based Q_e values in RCM12 compared to RCM4.5. Additionally, this explains why the land–ocean temperature contrast is higher in RCM4.5 compared to RCM12 in Fig. 11d. Although this bias may be important for the prediction of land surface variables and other related weather phenomena, for the current study it is adequate that the variations by MJO phase of the key variables is in broad agreement in RCM12 and RCM4.5.

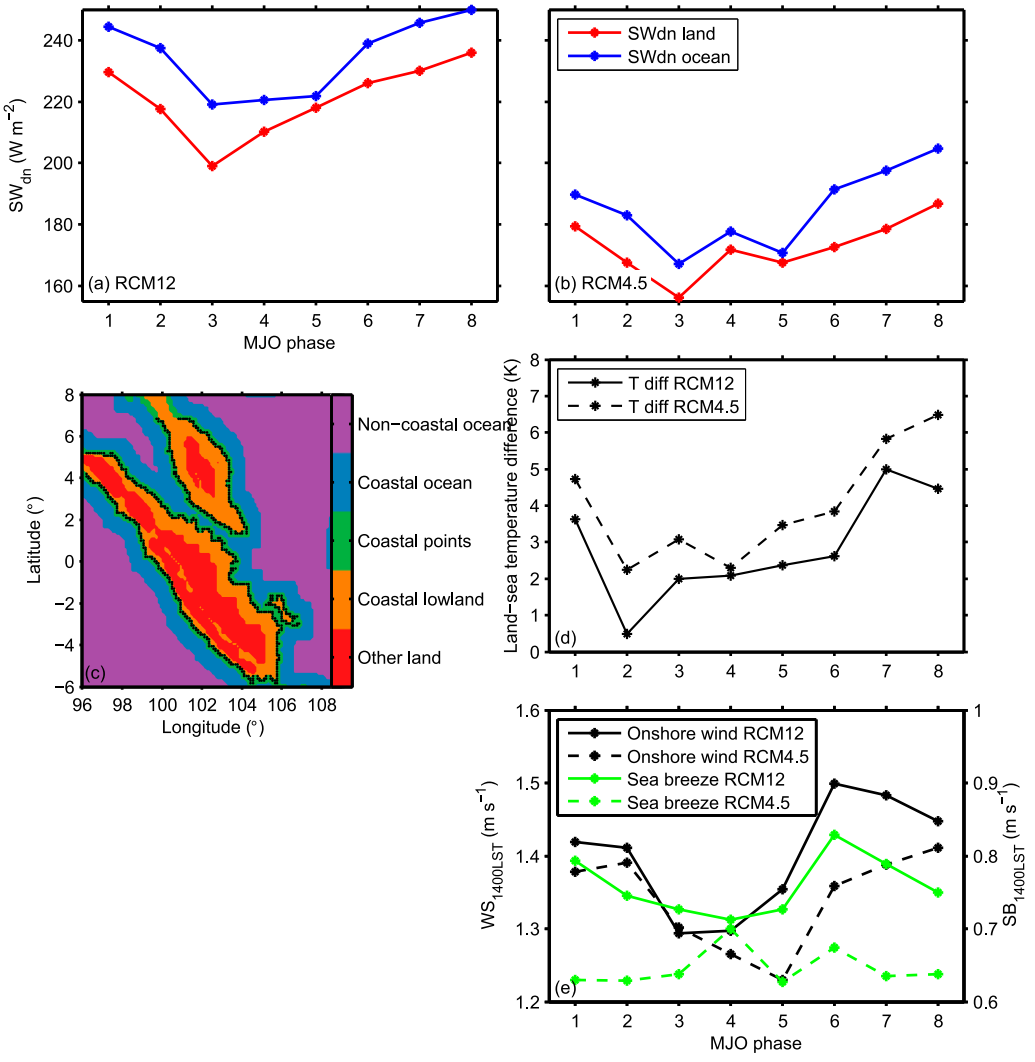

FIG. 11. Mean surface SW_{dn} radiative flux by MJO phase for (a) RCM12 and (b) RCM4.5. (c) The coastal ocean (blue) and coastal lowland (orange) classification used to compute the land–ocean temperature difference, and the coastal points (black dots) used to compute the onshore wind speeds and sea breeze for RCM12. Coastal is defined as within 120 km of the coastline and lowland as 500 m below mean sea level. Note that a number of the smaller islands have been removed for this analysis. (d) The surface temperature difference at 1400 LST between coastal lowland and coastal ocean; (e) the mean onshore 10-m wind speed ($WS_{1400LST}$, black lines) and the mean 10-m sea breeze ($SB_{1400LST}$, green lines), both by MJO phase at 1400 LST.

4. Synthesis of large-scale and mesoscale processes

This section synthesizes the results from section 3 in order to quantify the relative contributions of large-scale and mesoscale processes to the land–ocean rainfall differences by MJO phase over the MC. The variation of key variables by MJO phase is summarized in Fig. 13 for RCM12 (RCM4.5 is very similar). Figure 14 presents an overview of the regional rainfall anomalies along with schematics of idealized island cross sections for phases 1, 3, 4, and 6. These phases were selected to represent the key land–ocean differences in rainfall anomalies through the MJO cycle.

Phase 1 occurs before the arrival of the main MJO convective envelope (Fig. 13a), when there is a negative rainfall anomaly over the ocean and a positive rainfall anomaly over the western MC islands. There are prevailing easterlies at this time, with weak moisture flux convergence into the domain (Fig. 13c) and moderate θ_e (Fig. 13d). Figure 13e shows boundary layer (925 hPa) θ_e at 1300 LST minus θ_{es} at 600 hPa, which is a measure of the stability of the profile, where positive values indicate unstable profiles, with a high potential for convection. In phase 1 the profile is moderately unstable; this along with a low oceanic Q_e over

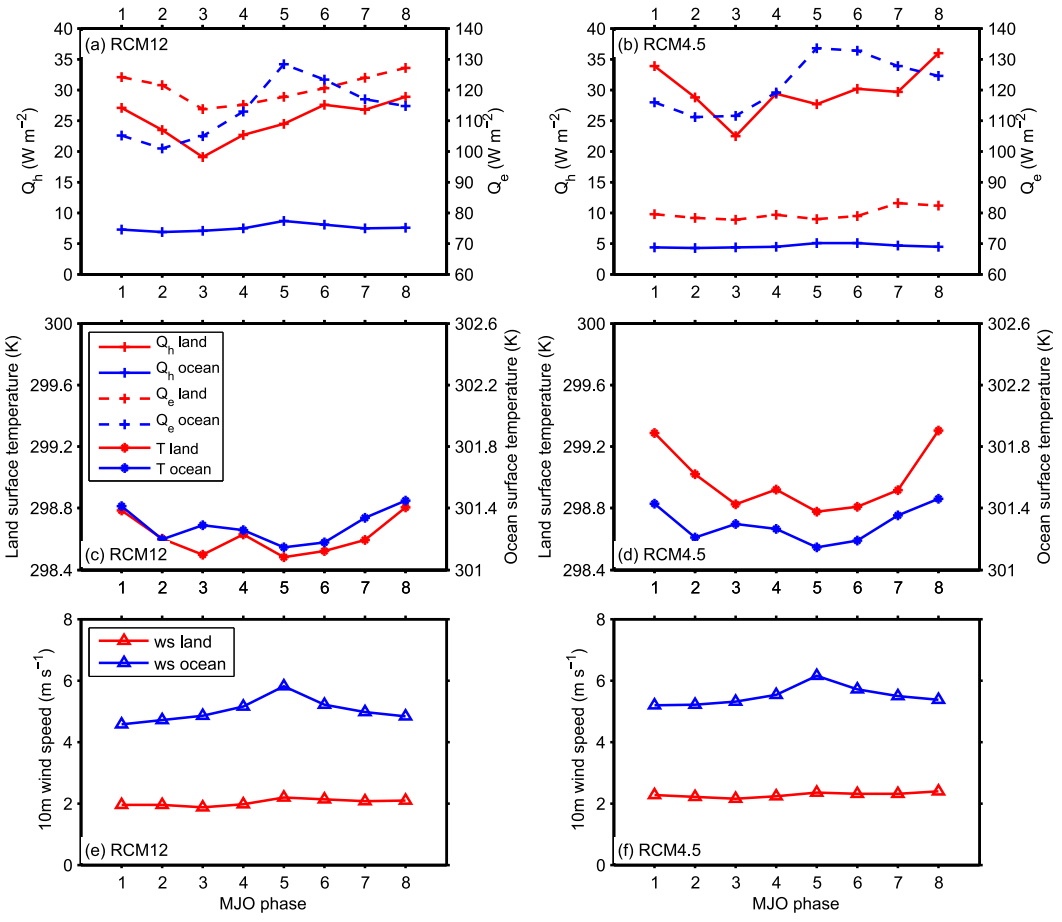

FIG. 12. (a),(b) Domain-mean Q_h and Q_e, (c),(d) surface temperature, and (e),(f) 10-m wind speed by MJO phase, averaged separately over land and ocean.

results in low rainfall over the ocean. Over land, however, SW_{dn} (Fig. 13f) and land-based Q_h (Fig. 13i) are high, which drives a strong onshore flow (Fig. 13g) that provides the low-level convergence necessary to sustain land-based convection and produce a positive rainfall anomaly over land.

In phase 2 the active envelope of the MJO is immediately to the west of the MC. The large-scale and mesoscale indicators in Fig. 13 and the land–ocean rainfall differences are all similar to those in phase 1. The exception is the moisture flux convergence, which peaks in phase 2. However, the moisture takes some time to build within the domain, explaining why θ_e does not peak until phase 3. By phase 3 the convective envelope of the MJO has arrived in the western MC, and high θ_e and high instability allow high rainfall to prevail throughout the domain. Surface heating through insolation and the strength of the onshore flow is low at this time, but the favorable large-scale convective environment allows rainfall to remain high over the land.

The convective MJO envelope remains over the western MC in phase 4, but moisture flux convergence is significantly reduced, leading to a reduction back to moderate θ_e. A wet anomaly in the oceanic rainfall occurs in this phase because of the increased oceanic Q_e, and high instability remains in the profile. Over the land, however, rainfall rates are greatly reduced because large-scale conditions are not sufficient to maintain wetter than average conditions without the presence of strong mesoscale triggers. In phase 5 the moisture flux convergence becomes negative (moisture flux divergence) and θ_e and atmospheric instability are greatly reduced. Oceanic precipitation remains high because a high oceanic Q_e ($\sim$130 W m^{-2}), caused by the peak in 10-m wind speeds in this phase, feeds the convection. By comparison, the phase 2 peak in moisture flux convergence is approximately 6 mm day^{-1}, which is equivalent to approximately 130 W m^{-2} (second axis of Fig. 13c). The high oceanic Q_e in phase 5 therefore almost exactly compensates for the lack of moisture provided by

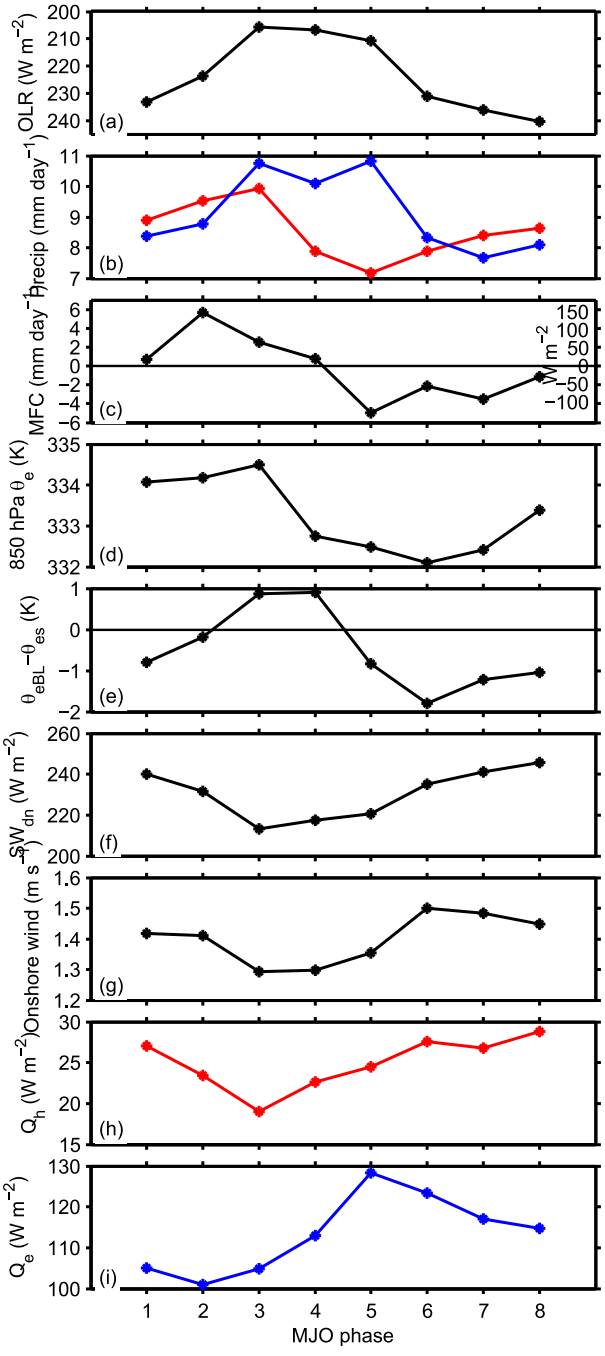

FIG. 13. Summary of the behavior of key variables by MJO phase, using RCM12 as an example. Black lines are domain means, and red and blue lines are means over land and sea, respectively. The difference $\theta_{eBL} - \theta_{es}$ is θ_e in the boundary layer (925 hPa) at 1300 LST minus θ_{es} at 600 hPa.

advection in this phase. Land-based precipitation is at its minimum in phase 5 because of the unfavorable large-scale conditions, low Q_e, and the lack of mesoscale triggers.

Phases 6 and 7 are the main suppressed MJO phases over the MC, where rainfall rates over both land and sea are anomalously low. This is caused by unfavorable large-scale conditions (negative moisture flux convergence, low θ_e, and low instability). Cloud cover is much reduced in these phases and thus SW_{dn} and the onshore flow reintensify. The presence of the reinvigorated mesoscale circulation does not, however, force high rainfall rates because the large-scale environment is not favorable. By phase 8 the moisture flux divergence is reduced to near zero and θ_e begins to increase again, setting up the environment for the next MJO cycle.

5. Conclusions

The study has utilized state-of-the-art RCM simulations to better understand the interaction between the large-scale environment and mesoscale processes associated with convection within the MJO. Two 10-yr RCM simulations over the western MC were utilized with horizontal grid spacings small enough to adequately represent key mesoscale features such as coastlines, topographic variations, and the land/sea breeze. Convection was parameterized in one simulation (RCM12), and in the other the convective parameterization was switched off and convection was permitted to develop explicitly (RCM4.5). For the first time we have gained the ability to run these types of simulations for periods that are sufficiently long to statistically analyze the interaction between mesoscale circulations and a mode of intraseasonal variability.

The RCM simulations and observations were used to test a hypothesis that explains the reasons for differences in the mean rainfall anomaly over land and sea by MJO phase over the MC. Using satellite-derived brightness temperature and rainfall, Peatman et al. (2014) suggest that this difference is a combination of variability by MJO phase of 1) the large-scale environment, forced by equatorial wave dynamics and 2) land–ocean temperature contrasts through surface insolation, resulting in the varying strength of mesoscale convective triggers. They could not provide sufficient evidence to support this hypothesis because they lacked observational and/or model datasets with sufficient duration and spatial resolution.

The synthesis of observational and model results from this study has resulted in some key conclusions regarding the behavior and cause of convection within the MC region, which support the hypothesis of Peatman et al. (2014). Solar insolation is reduced during the active phases of the MJO when cloud cover is at a maximum. This reduces the daytime onshore flow that is controlled by a combination of the sea breeze circulation, upslope

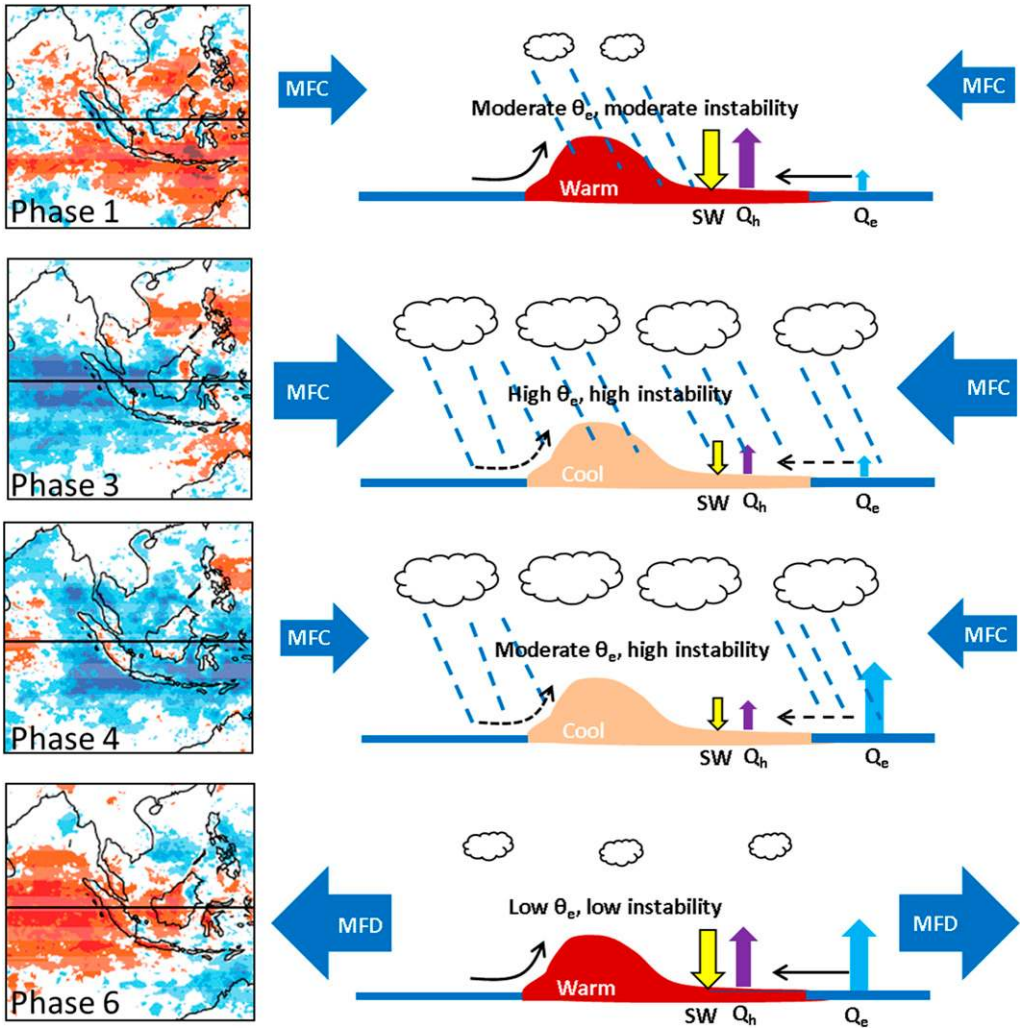

FIG. 14. Schematic illustrating the interaction between domain-mean conditions that are controlled by the larger-scale circulation and mesoscale circulations that are controlled by more local processes and how this impacts rainfall distribution by MJO phase. The contour plots on the left-hand side show observed daily mean precipitation anomalies from Peatman et al. (2014) for MJO phases 1, 3, 4, and 6. The schematics on the right-hand side represent idealized ocean–land–ocean cross sections through an MC island. The large blue arrows represent domain-scale MFC or moisture flux divergence (MFD), and the domain-mean θ_e is given in the center of the cross sections. The light blue, purple, and yellow arrows represent ocean-based Q_e, land-based Q_h, and domain-mean SW_{dn} fluxes, respectively. The size of the arrows relative to other arrows of the same type indicates the relative strength or magnitude of a given variable. The thin black solid (dashed) lines indicate stronger (weaker) afternoon onshore flows.

mountain winds, and the synoptic-scale circulation, which are thought to be major convective triggers over the MC region (Qian 2008). Equatorial wave dynamics control the larger-scale convective environment by controlling the amount of moisture transported into the MC region, the atmospheric stability, and the oceanic latent heat flux through moderation of the near-surface wind speed. The interaction of the large scale and mesoscale explains the land–ocean rainfall anomaly differences by MJO phase (i.e., why land-based rainfall peaks in an earlier MJO phase compared to over the ocean).

One might expect that the largest rainfall rates over the MC occur over both land and sea in the phases with the highest θ_e and/or highest atmospheric instability. This is true over the ocean, where surface-based triggers such as the sea breeze are weak and the large-scale environment, forced by equatorial wave dynamics (e.g., Hendon and Salby 1994; Maloney and Hartmann 1998; Matthews 2000), is the dominant control of convection.

The latent heat flux is also a dominant control in the late active phases (phase 5). The large-scale environment becomes less favorable at this time, but convection is fed through high surface winds, as described by the wind-induced surface heat exchange (WISHE) mechanism (Emanuel 1987; Neelin et al. 1987), that lead to about 30% increases in oceanic Q_e. This 30% increase provides a similar amount of moisture as that provided by the moisture flux convergence in phase 2.

Behavior over the land is different; both the large-scale environment and the mesoscale circulations that act as convective triggers are major controls on convection. Convection is at its maximum when θ_e and atmospheric instability are at their highest (phase 3), even though the onshore flow is weak at this time. In the subsequent two phases θ_e and atmospheric instability decrease, yet the cloud cover remains high, which reduces the onshore flow and significantly decreases convection. In phases 1 and 2, before the active convective envelope is overhead, the land-based rainfall anomalies are larger than over the ocean. This is because the strong onshore flow is able to force rainfall, even when the large-scale environment is only moderately favorable for convection. It is worth emphasizing at this point that the MC is one of the wettest places on Earth and that even in the driest MJO phases domain-mean rainfall does not decrease below 7 mm day^{-1}. The relative importance of the large-scale environment and mesoscale circulations are in controlling wet and dry anomalies, rather than wet and dry periods.

The second aim of this study was to evaluate the ability of the RCMs to represent key processes relating to the MJO, such as rainfall and the large-scale convective environment. Both RCMs are wetter than TRMM over the ocean in the southwestern part of the averaging domain, where model–observation differences are up to 10 mm day^{-1}. Both RCMs are also drier than TRMM elsewhere in the domain. RCM4.5 is also wetter than TRMM over the high orography, which is a well-known issue with the Met Office CP model and is the subject of ongoing research at the Met Office. Both RCMs were able to reproduce the propagation of storms off southwestern Sumatra, although the bias in the timing of the diurnal cycle of rainfall in models with parameterized convection, where the diurnal peak over land occurs around the solar maximum, rather than in the early evening, is clear in the RCM12, with significant improvements in RCM4.5.

The variation in domain-mean OLR, winds, θ_e, and stability by MJO phase are very similar in the two simulations and compared to observations, which indicates that the LBCs have a strong influence on the circulation and moisture transport within the regional domains. Both RCMs reproduce the overall variation in mean rainfall and diurnal amplitude by MJO phase, which shows that the convection in the RCMs is able to respond to the variability of the large-scale and mesoscale environments. The oceanic rainfall is not as well represented as over land; the diurnal amplitude by MJO is quite static and the phases of peak oceanic rainfall are not identical to those observed, although like observations, the peak over the ocean occurs in a later phase than that over the land in both RCMs. Both RCMs produce similar variations by MJO phase in insolation, land–ocean temperature contrasts, onshore flow strength, and surface heat fluxes. There are, however, differences in the absolute magnitudes of some of these variables. As demonstrated by Birch et al. (2015) the peak in rainfall during the middle of the day in RCM12, caused by the well-known convective parameterization bias, leads to the boundary layer being cooler and moister than RCM4.5, which reduces the surface temperature, increases the land-based latent heat flux, and decreases the land-based sensible heat flux.

Overall model performance was certainly adequate enough to be confident of the conclusions made in this study. The fact that the two RCMs behave in a broadly similar way suggests that the results are reasonably insensitive to choices in model configuration such as the method for representing convection, domain size, and resolution, which increases confidence in the results. What is perhaps surprising is that, in terms of anomalies by MJO phase, the convection-permitting simulation (RCM4.5) did not significantly outperform the convection-parameterized simulation (RCM12). Recent results from the Cascade project showed that convection-permitting models were able to perform much better in aspects such as the diurnal cycle, the sensitivity to convective triggers such as low-level convergence, and the propagation and organization of convection over West Africa (Pearson et al. 2014; Birch et al. 2014b). One may have expected that the improved performance of RCM4.5 compared with RCM12 in terms of the diurnal cycle of convection would have had a greater impact on the results here. The step change in the ability of convection-permitting models to represent convection as demonstrated in the Cascade project does, however, appear to be much more significant over continental regions such as West Africa. The improvements in convection-permitting configurations over oceanic regions are much smaller (Holloway et al. 2013). The mixed land and ocean surface types of the Maritime Continent may be one reason why the performance of RCM4.5 was in many ways no better than RCM12. The two RCMs also behaved in a similar way

because both simulations are evidently very strongly forced by their boundary conditions, and the results of this study suggest that large-scale forcing plays a major role in defining the characteristics of convection and rainfall over the Maritime Continent.

Although the way convection is represented in the RCMs does not appear to play a major role in defining how the MJO impacts convection over the Maritime Continent, it may be crucial for correctly representing the upscale feedback of convection in the Maritime Continent on the MJO. Because of computational expense, the model domain is relatively small in the current study and thus the convection is highly constrained by the boundary conditions. Such constraints mean that, while likely important for the propagation of the MJO, the upscale impact of Maritime Continent convection could not be assessed in this study and is planned for future work.

Acknowledgments. We are grateful to Meteorological Service Singapore for allowing access to the regional climate model simulations. Many thanks to Jill Johnson for advising on statistical methods. We are grateful to Matthew Wheeler for providing the MJO index (http://cawcr.gov.au/staff/mwheeler/maproom/RMM/). We acknowledge the TRMM scientists and associated NASA personnel for the production of the TRMM data used in this paper and are grateful to the Goddard Earth Sciences (GES) Data and Information Services Center (DISC) for making the data available. We are grateful to NOAA for providing access to the radiosonde observations. This work made use of the facilities of MONSooN, a supercomputer jointly funded by the Natural Environmental Research Council and the Met Office. The authors thank three anonymous reviewers for their helpful comments and suggestions.

REFERENCES

Best, M. J., and Coauthors, 2011: The Joint UK Land Environment Simulator (JULES), model description—Part 1: Energy and water fluxes. *Geosci. Model Dev.*, **4**, 677–699, doi:10.5194/gmd-4-677-2011.

Birch, C. E., J. H. Marsham, D. J. Parker, and C. M. Taylor, 2014a: The scale dependence and structure of convergence fields preceding the initiation of deep convection. *Geophys. Res. Lett.*, **41**, 4769–4776, doi:10.1002/2014GL060493.

——, D. J. Parker, J. H. Marsham, D. Copsey, and L. Garcia-Carreras, 2014b: A seamless assessment of the role of convection in the water cycle of the West African monsoon. *J. Geophys. Res.*, **119**, 2890–2912, doi:10.1002/2013JD020887.

——, M. Roberts, L. Garcia-Carreras, D. Ackerley, M. Reeder, A. Lock, and R. Schiemann, 2015: Sea-breeze dynamics and convection initiation: The influence of convective parameterization in weather and climate model biases. *J. Climate*, **28**, 8093–8108, doi:10.1175/JCLI-D-14-00850.1.

Boutle, I. A., J. E. J. Eyre, and A. P. Lock, 2014: Seamless stratocumulus simulation across the turbulent gray zone. *Mon. Wea. Rev.*, **142**, 1655–1668, doi:10.1175/MWR-D-13-00229.1.

Chen, S. S., and R. A. Houze Jr., 1997: Diurnal variation and lifecycle of deep convective systems over the tropical Pacific warm pool. *Quart. J. Roy. Meteor. Soc.*, **123**, 357–388, doi:10.1002/qj.49712353806.

Dai, A., 2006: Precipitation characteristics in eighteen coupled climate models. *J. Climate*, **19**, 4605–4630, doi:10.1175/JCLI3884.1.

——, X. Lin, and K.-L. Hsu, 2007: The frequency, intensity, and diurnal cycle of precipitation in surface and satellite observations over low- and mid-latitudes. *Climate Dyn.*, **29**, 727–744, doi:10.1007/s00382-007-0260-y.

Dee, D. P., and Coauthors, 2011: The ERA-Interim reanalysis: Configuration and performance of the data assimilation system. *Quart. J. Roy. Meteor. Soc.*, **137**, 553–597, doi:10.1002/qj.828.

Del Genio, A. D., Y. Chen, D. Kim, and M.-S. Yao, 2012: The MJO transition from shallow to deep convection in *CloudSat*/CALIPSO data and GISS GCM simulations. *J. Climate*, **25**, 3755–3770, doi:10.1175/JCLI-D-11-00384.1.

Donlon, C. J., M. Martin, J. D. Stark, J. Roberts-Jones, E. Fiedler, and W. Wimmer, 2012: The operational sea surface temperature and sea ice analysis (OSTIA). *Remote Sens. Environ.*, **116**, 140–158, doi:10.1016/j.rse.2010.10.017.

ECMWF, 2015: ERA-Interim, daily. ECMWF, accessed 1 June 2015. [Available online at http://apps.ecmwf.int/datasets/data/interim-full-daily].

Emanuel, K., 1987: An air–sea interaction model of intraseasonal oscillations in the tropics. *J. Atmos. Sci.*, **44**, 2324–2340, doi:10.1175/1520-0469(1987)044<2324:AASIMO>2.0.CO;2.

Essery, R. L. H., M. J. Best, and P. M. Cox, 2001: MOSES 2.2 technical documentation. Met Office Hadley Centre Tech. Note 30, 30 pp. [Available online at http://www.metoffice.gov.uk/media/pdf/9/j/HCTN_30.pdf.]

Gregory, D., and P. R. Rowntree, 1990: A mass flux convection scheme with representation of cloud ensemble characteristics and stability-dependent closure. *Mon. Wea. Rev.*, **118**, 1483–1506, doi:10.1175/1520-0493(1990)118<1483:AMFCSW>2.0.CO;2.

Hassim, M. E. E., T. P. Lane, and W. W. Grabowski, 2016: The diurnal cycle of rainfall over New Guinea in convection-permitting WRF simulations. *Atmos. Chem. Phys.*, **16**, 161–175, doi:10.5194/acp-16-161-2016.

Hendon, H. H., and M. L. Salby, 1994: The life cycle of the Madden–Julian oscillation. *J. Atmos. Sci.*, **51**, 2225–2237, doi:10.1175/1520-0469(1994)051<2225:TLCOTM>2.0.CO;2.

Holloway, C. E., S. J. Woolnough, and G. M. S. Lister, 2012: Precipitation distributions for explicit versus parametrized convection in a large-domain high-resolution tropical case study. *Quart. J. Roy. Meteor. Soc.*, **138**, 1692–1708, doi:10.1002/qj.1903.

——, ——, and ——, 2013: The effects of explicit versus parameterized convection on the MJO in a large-domain high-resolution tropical case study. Part I: Characterization of large-scale organization and propagation. *J. Atmos. Sci.*, **70**, 1342–1369, doi:10.1175/JAS-D-12-0227.1.

Huffman, G. J., and Coauthors, 2007: The TRMM Multisatellite Precipitation Analysis: Quasi-global, multiyear, combined-sensor precipitation estimates at fine scales. *J. Hydrometeor.*, **8**, 38–55, doi:10.1175/JHM560.1.

Jin, F., and B. J. Hoskins, 1995: The direct response to tropical heating in a baroclinic atmosphere. *J. Atmos. Sci.*, **52**, 307–319, doi:10.1175/1520-0469(1995)052<0307:TDRTTH>2.0.CO;2.

Johnson, S. J., and Coauthors, 2016: The resolution sensitivity of the South Asian Monsoon and Indo-Pacific in a global 0.35° AGCM. *Climate Dyn.*, **46**, 807–831, doi:10.1007/s00382-015-2614-1.

Kendon, E. J., N. M. Roberts, C. A. Senior, and M. J. Roberts, 2012: Realism of rainfall in a very high-resolution regional climate model. *J. Climate*, **25**, 5791–5806, doi:10.1175/JCLI-D-11-00562.1.

Kiladis, G. N., K. H. Straub, and P. T. Haertel, 2005: Zonal and vertical structure of the Madden–Julian oscillation. *J. Atmos. Sci.*, **62**, 2790–2809, doi:10.1175/JAS3520.1.

Kim, D., A. H. Sobel, E. D. Maloney, D. M. W. Frierson, and I.-S. Kang, 2011: A systematic relationship between intraseasonal variability and mean state bias in AGCM simulations. *J. Climate*, **24**, 5506–5520, doi:10.1175/2011JCLI4177.1.

Lin, J.-L., and Coauthors, 2006: Tropical intraseasonal variability in 14 IPCC AR4 climate models. Part I: Convective signals. *J. Climate*, **19**, 2665–2690, doi:10.1175/JCLI3735.1.

Lock, A. P., A. R. Brown, M. R. Bush, G. M. Martin, and R. N. B. Smith, 2000: A new boundary layer mixing scheme. Part I: Scheme description and single-column model tests. *Mon. Wea. Rev.*, **128**, 3187–3199, doi:10.1175/1520-0493(2000)128<3187:ANBLMS>2.0.CO;2.

Love, B. S., A. J. Matthews, and G. M. S. Lister, 2011: The diurnal cycle of precipitation over the Maritime Continent in a high-resolution atmospheric model. *Quart. J. Roy. Meteor. Soc.*, **137**, 934–947, doi:10.1002/qj.809.

Maloney, E. D., and D. L. Hartmann, 1998: Frictional moisture convergence in a composite life cycle of the Madden–Julian oscillation. *J. Climate*, **11**, 2387–2403, doi:10.1175/1520-0442(1998)011<2387:FMCIAC>2.0.CO;2.

Martin, G. M., M. A. Ringer, V. D. Pope, A. Jones, C. Dearden, and T. J. Hinton, 2006: The physical properties of the atmosphere in the new Hadley Centre Global Environmental Model (HadGEM1). Part I: Model description and global climatology. *J. Climate*, **19**, 1274–1301, doi:10.1175/JCLI3636.1.

Matthews, A. J., 2000: Propagation mechanisms for the Madden-Julian Oscillation. *Quart. J. Roy. Meteor. Soc.*, **126**, 2637–2651, doi:10.1002/qj.49712656902.

——, G. Pickup, S. C. Peatman, P. Clews, and J. Martin, 2013: The effect of the Madden-Julian oscillation on station rainfall and river level in the Fly River system, Papua New Guinea. *J. Geophys. Res.*, **118**, 10 926–10 935, doi:10.1002/jgrd.50865.

Mizielinski, M. S., and Coauthors, 2014: High-resolution global climate modelling: The UPSCALE project, a large simulation campaign. *Geosci. Model Dev.*, **7**, 563–591, doi:10.5194/gmdd-7-563-2014.

Mori, S., and Coauthors, 2004: Diurnal land–sea rainfall peak migration over Sumatera Island, Indonesian Maritime Continent, observed by TRMM satellite and intensive rawinsonde soundings. *Mon. Wea. Rev.*, **132**, 2021–2039, doi:10.1175/1520-0493(2004)132<2021:DLRPMO>2.0.CO;2.

Moron, V., A. W. Robertson, J.-H. Qian, and M. Ghil, 2015: Weather types across the Maritime Continent: From the diurnal cycle to interannual variations. *Front. Env. Sci*, **2**, doi:10.3389/fenvs.2014.00065.

NASA, 2015: Tropical Rainfall Measuring Mission brightness temperature and 3B42 precipitation product, version 7. NASA Goddard Earth Sciences Data and Information Service Center, accessed 28 August 2014. [Available online at http://disc.sci.gsfc.nasa.gov/precipitation/documentation/TRMM_README/TRMM_3B42_readme.shtml.]

Neale, R., and J. Slingo, 2003: The Maritime Continent and its role in global climate: A GCM study. *J. Climate*, **16**, 834–848, doi:10.1175/1520-0442(2003)016<0834:TMCAIR>2.0.CO;2.

Neelin, J., I. Held, and K. Cook, 1987: Evaporation–wind feedback and low-frequency variability in the tropical atmosphere. *J. Atmos. Sci.*, **44**, 2341–2348, doi:10.1175/1520-0469(1987)044<2341:EWFALF>2.0.CO;2.

NOAA, 2015: Derived-v2 parameters computed from v1.20 data. NOAA/Integrated Global Radiosonde Archive, accessed 1 April 2015. [Available online at ftp://ftp.ncdc.noaa.gov/pub/data/igra/].

Oh, J.-H., K.-Y. Kim, and G.-H. Lim, 2012: Impact of MJO on the diurnal cycle of rainfall over the western Maritime Continent in the austral summer. *Climate Dyn.*, **38**, 1167–1180, doi:10.1007/s00382-011-1237-4.

Pearson, K. J., G. M. S. Lister, C. E. Birch, R. P. Allan, R. J. Hogan, and S. T. Woolnough, 2014: Modelling the diurnal cycle of tropical convection across the 'grey zone.' *Quart. J. Roy. Meteor. Soc.*, **140**, 491–499, doi:10.1002/qj.2145.

Peatman, S. C., A. J. Matthews, and D. P. Stevens, 2014: Propagation of the Madden–Julian oscillation through the Maritime Continent and scale interaction with the diurnal cycle of precipitation. *Quart. J. Roy. Meteor. Soc.*, **140**, 814–825, doi:10.1002/qj.2161.

——, ——, and ——, 2015: Propagation of the Madden–Julian oscillation and scale interaction with the diurnal cycle in a high-resolution GCM. *Climate Dyn.*, **45**, 2901–2918, doi:10.1007/s00382-015-2513-5.

Qian, J., 2008: Why precipitation is mostly concentrated over islands in the Maritime Continent. *J. Atmos. Sci.*, **65**, 1428–1441, doi:10.1175/2007JAS2422.1.

Rauniyar, S. P., and K. J. E. Walsh, 2011: Scale interaction of the diurnal cycle of rainfall over the Maritime Continent and Australia: Influence of the MJO. *J. Climate*, **24**, 325–348, doi:10.1175/2010JCLI3673.1.

Romilly, T. G., and M. Gebremichael, 2011: Evaluation of satellite rainfall estimates over Ethiopian river basins. *Hydrol. Earth Syst. Sci.*, **15**, 1505–1514, doi:10.5194/hess-15-1505-2011.

Saito, K., T. Keenan, G. Holland, and K. Puri, 2001: Numerical simulation of the diurnal evolution of tropical island convection over the Maritime Continent. *Mon. Wea. Rev.*, **129**, 378–400, doi:10.1175/1520-0493(2001)129<0378:NSOTDE>2.0.CO;2.

Stein, T. H. M., D. J. Parker, R. J. Hogan, C. E. Birch, C. E. Holloway, G. Lister, J. H. Marsham, and S. J. Woolnough, 2015: The representation of the West African monsoon vertical cloud structure in the Met Office Unified Model: An evaluation with *CloudSat*. *Quart. J. Roy. Meteor. Soc.*, **141**, 3312–3324, doi:10.1002/qj.2614.

Tseng, K.-C., C.-H. Sui, and T. Li, 2015: Moistening processes for Madden–Julian oscillations during DYNAMO/CINDY. *J. Climate*, **28**, 3041–3057, doi:10.1175/JCLI-D-14-00416.1.

Walters, D. N., and Coauthors, 2014: The Met Office Unified Model Global Atmosphere 4.0 and JULES Global Land 4.0 configurations. *Geosci. Model Dev.*, **7**, 361–386, doi:10.5194/gmd-7-361-2014.

Webster, S., S. Chan, M. E. Hassim, E. Kendon, C. Marzin, S. Sahany, and C. Scannell, 2015: Convective-scale modelling. Singapore's second national climate change study: Climate projections to 2100, Meteorological Service Singapore Rep., 1–21. [Available online at http://ccrs.weather.gov.sg/wp-content/uploads/2015/07/V2_Ch6_Convective_Scale_Modelling.pdf.]

Wheeler, M. C., and H. H. Hendon, 2004: An all-season real-time multivariate MJO index: Development of an index for moni-

toring and prediction. *Mon. Wea. Rev.*, **132**, 1917–1932, doi:10.1175/1520-0493(2004)132<1917:AARMMI>2.0.CO;2.

Wilson, D. R., and S. P. Ballard, 1999: A microphysically based precipitation scheme for the U.K. Meteorological Office unified model. *Quart. J. Roy. Meteor. Soc.*, **125**, 1607–1636, doi:10.1002/qj.49712555707.

——, A. C. Bushell, A. M. Kerr-Munslow, J. D. Price, and C. J. Morcrette, 2008a: PC2: A prognostic cloud fraction and condensation scheme. I: Scheme description. *Quart. J. Roy. Meteor. Soc.*, **134**, 2093–2107, doi:10.1002/qj.333.

——, ——, ——, ——, ——, and A. Bodas-Salcedo, 2008b: PC2: A prognostic cloud fraction and condensation scheme. II: Climate model simulations. *Quart. J. Roy. Meteor. Soc.*, **134**, 2109–2125, doi:10.1002/qj.332.

Wood, N., and Coauthors, 2014: An inherently mass-conserving semi-implicit semi-Lagrangian discretization of the deep-atmosphere global non-hydrostatic equations. *Quart. J. Roy. Meteor. Soc.*, **140**, 1505–1520, doi:10.1002/qj.2235.

Zhang, C., 2005: Madden-Julian oscillation. *Rev. Geophys.*, **43**, RG2003, doi:10.1029/2004RG000158.